

CCCP OB Signatures Paper, September 8, 2021

Carina OB Stars: X-ray Signatures of Wind Shocks and Magnetic Fields

Marc Gagné, Garrett Fehon, and Michael R. Savoy

Department of Geology and Astronomy, West Chester University, West Chester, PA 19383

David H. Cohen

Department of Physics and Astronomy, Swarthmore College, Swarthmore, PA 19081

Leisa K. Townsley, Patrick S. Broos, and Matthew S. Povich¹

Department of Astronomy & Astrophysics, 525 Davey Laboratory, Pennsylvania State University, University Park, PA 16802

Michael F. Corcoran

CRESST and X-ray Astrophysics Laboratory, NASA/GSFC, Greenbelt, MD 20771

Nolan R. Walborn

Space Telescope Science Institute, Baltimore, MD 21218, USA

Nancy Remage Evans

Smithsonian Astrophysical Observatory, MS 4, 60 Garden St., Cambridge, MA 02138

Anthony F.J. Moffat

Département de Physique, Université de Montréal, Succursale Centre-Ville, Montréal, QC, H3C 3J7, Canada

Yaël Nazé²

GAPHE, Département AGO, Université de Liège, Allée du 6 Août 17, Bat. B5C, B4000-Liège, Belgium and Research Associate FRS-FNRS

and

Lida M. Oskinova

Institute for Physics and Astronomy, University of Potsdam, 14476 Potsdam, Germany

ABSTRACT

The *Chandra* Carina Complex contains 200 known O- and B type stars. The *Chandra* survey detected 68 of the 70 O stars and 61 of 127 known B0-B3 stars. We have assembled a publicly available optical/X-ray database to identify OB stars that depart from the canonical L_X/L_{bol} relation, or whose average X-ray temperatures exceed 1 keV. Among the single O stars with high kT we identify two candidate magnetically confined wind shock sources: Tr16-22, O8.5 V, and LS 1865, O8.5 V((f)). The O4 III(fc) star HD 93250 exhibits strong, hard, variable X-rays, suggesting it may be a massive binary with a period of > 30 days. The visual O2 If* binary HD 93129A shows soft 0.6 keV and hard 1.9 keV emission components, suggesting embedded wind shocks close to the O2 If* Aa primary, and colliding wind shocks between Aa and Ab. Of the 11 known O-type spectroscopic binaries, the long orbital-period systems HD 93343, HD 93403 and QZ Car have higher shock temperatures than short-period systems such as HD 93205 and FO 15. Although the X-rays from most B stars may be produced in the coronae of unseen, low-mass pre-main sequence companions, a dozen B stars with high L_X cannot be explained by a distribution of unseen companions. One of these, SS73 24 in the Treasure Chest cluster, is a new candidate Herbig Be star.

Subject headings: X-rays: stars — stars: early-type — open clusters and associations: individual: Cl Bochum 10, Cl Bochum 11, Cl Collinder 228, Cl Trumpler 14, Cl Trumpler 15, Cl Trumpler 16 — stars: individual: HD 93250, HD 93129A, HD 93403, HD 93205, HD 93343, QZ Car, SS73 24, FO 15, Cl Trumpler 16 22, CPD-59 2610, HD 93501

1. Introduction

The *Chandra* Carina Complex Project (CCCP) (Townesley et al. 2011a) survey area contains over 200 massive stars: the luminous blue variable (LBV) η Car, the Wolf Rayet (WR) stars WR 22, WR 24 and WR 25, 70 known O stars, and 127 B0-B3 stars with determined spectral types and photometry consistent with a distance of 2.3 kpc to the Carina cluster Trumpler 16 (Tr 16) (Smith 2006). In the next section we describe the database of

¹NSF Astronomy & Astrophysics Postdoctoral Fellow

²Research Associate FRS-FNRS

OB stars in more detail. Briefly, the massive star population in Carina can be divided into groups based on spectral type, luminosity class and binarity: LBV/WR stars (4), early-O binaries (6), early-O single dwarfs and giants (10), late-O binaries (9), late-O dwarfs and giants (44), single O-type supergiants (1), B0-B3 stars (127), and B5-B7 stars (3).

In addition to the OB stars with measured spectral types considered here and by Nazé et al. (2011), this volume contains four other articles which discuss the massive-star population in Carina: Povich et al. (2011a) present a list of 94 candidate OB stars, selected on basis on their X-ray emission and infrared spectral energy distributions (SED); their spectral types have not been determined. Evans et al. (2011) identify candidate late-B stars in Tr 16 based on their UBV photometry. Townsley et al. (2011a) analyze the CCCP spectra of the three WR stars and Parkin et al. (2011) present a detailed X-ray spectral/temporal analysis of the double spectroscopic binary QZ Car, O9.7 I + O8 III. In this paper, we examine the X-ray, optical, and infrared characteristics of the 200 OB stars with determined spectral types and use X-ray spectra and light curves of this large sample of well-studied OB stars to better understand the physical mechanisms that produce X-rays in massive stellar systems.

The ubiquitous X-ray emission from O and early B stars is generally thought to arise in shocks embedded in the powerful radiation-driven winds of these stars. However, there are exceptions to this paradigm, with a subset of early-type stars showing harder and stronger X-ray emission than can be explained by embedded wind shocks (EWS) alone. We point to three recent X-ray surveys that have examined these questions in some detail: the *XMM-Newton* survey of NGC 6231 in the Sco OB1 association (Sana et al. 2006a,b), the *Chandra* survey of Tr 16 (Evans et al. 2003, 2004), and the *Chandra* Orion Ultradeep Project (Stelzer et al. 2005).

The Orion Nebula Cluster contains only two O stars, and both have unusual X-ray emission: θ^1 Ori C, O7 Vp (Gagné et al. 2005), and θ^2 Ori A, O9.5 SB (Feigelson et al. 2002; Schulz et al. 2006). Of the early-B stars, Stelzer et al. (2005) identify two groups: strong-wind sources (earlier than B4) that give rise to X-rays in wind shocks (relevant to this study), and weak-wind sources (later than B4) whose X-rays, when detected, may be produced by late-type pre-main-sequence (PMS) companions (see Evans et al. 2011).

In their study of Tr 16 and part of Trumpler 14 (Tr 14), Evans et al. (2003, 2004) analyzed the ACIS-I spectra of some of the prominent O stars in Carina, identifying HD 93250, O4 III(fc), and Tr16-244, O3/4 I, as highly unusual, and proposing a new colliding-wind binary system: Tr16-22, O8.5 V. Aside from these anomalously active stars, Evans et al. (2003) find that the canonical $L_X \approx 10^{-7} L_{\text{bol}}$ relationship is obeyed.

In their comprehensive study of the OB stars in NGC 6231, Sana et al. (2006b) confirm

the L_X/L_{bol} relationship in the soft *XMM-Newton* bands below 2.5 keV, but show a breakdown in the correlation in the 2.5-10 keV hard band. They also confirm the prominent kink in L_X/L_{bol} below $\log L_{\text{bol}} = 38$ first noted by Berghoefer et al. (1997) (see also Nazé et al. 2011).

In this paper, we focus mainly on three emission mechanisms, in addition to EWS, to understand the X-rays observed from O and B stars in the CCCP: colliding wind shocks (CWS), magnetically confined wind shocks (MCWS), and coronal emission from unseen pre-main-sequence (PMS) companions, though we discuss other mechanisms in §1.5. In particular, we focus on those stars that show high L_X/L_{bol} , hard X-ray spectra, or show notable time variability.

1.1. Embedded Wind Shocks

The default mechanism for X-ray production on O and early B stars is embedded wind shocks (EWS), generally assumed to be associated with the Doppler deshadowing instability intrinsic to line driving (Lucy & White 1980; Lucy 1982; Owocki et al. 1988; Feldmeier et al. 1997). The instability predicts that wind streams having different velocities interact, shock heating a modest fraction of the wind beyond a few tenths of a stellar radius. Several stellar radii above the photosphere, the shocked portion of the wind is traveling at speeds approaching the wind terminal velocity of thousands of km s^{-1} . (Dessart & Owocki 2005a,b).

But the relative velocities of the interacting wind streams are generally only a few hundred km s^{-1} , generating shock temperatures of just a few million K. This shock-heated plasma radiates a line-dominated soft X-ray spectrum. This soft X-ray emission generally shows little variability, indicating that there are numerous separate shock-heated regions of the wind at any given time. Wind clumping is a universal phenomenon in hot-star winds (Lépine & Moffat 1999; Lépine et al. 2000; Moffat 2008) and Feldmeier et al. (2003) showed that the wind clumping affects the emergent X-ray line profiles.

The soft X-ray emission is attenuated by the colder, X-ray absorbing wind in which it is embedded. This wind attenuation affects the shapes of individual line profiles, as is evident in high-resolution X-ray spectroscopic studies of nearby O stars, which also confirm Doppler broadening commensurate with the wind terminal velocity, lending strong support to the EWS mechanism (Kahn et al. 2001; Cassinelli et al. 2001; Zhekov & Palla 2007; Walborn et al. 2009; Cohen et al. 2010).

The wind attenuation can harden the overall X-ray spectrum for early O stars with very high mass-loss rates. The attenuation of the X-rays from embedded wind shocks also

affects the emergent X-ray luminosity. Empirically, a scaling of emergent X-ray luminosity with bolometric luminosity, $L_X \approx 10^{-7} L_{\text{bol}}$, has been long known (Pallavicini et al. 1981), and is largely confirmed in the broad OB population in the CCCP (Nazé et al. 2011). No strong theoretical expectation for this scaling has been found, although wind attenuation can explain it in principle (Owocki & Cohen 1999).

For Carina O stars with X-ray emission dominated by the EWS mechanism, we should expect to see soft X-ray emission (characterized by $kT < 1$ keV) at a level corresponding to $L_X \approx 10^{-7} L_{\text{bol}}$, and with little variability. For B stars, significantly lower relative X-ray luminosities are seen, with values as low as $L_X \approx 10^{-9} L_{\text{bol}}$ by spectral subtype B2 V (Cohen et al. 1997).

While embedded wind shocks presumably exist in all early-type stars with strong radiation-driven winds, detailed X-ray studies of nearby O and early B stars show that a fraction of them have properties that are at odds with the EWS scenario. These usually involve higher X-ray luminosities and harder X-ray spectra than is predicted to arise in embedded wind shocks alone, and often involve X-ray time variability on orbital or rotational timescales. When high-resolution X-ray spectra are available, these often show narrower X-ray emission lines, as well. Corroborating evidence from other wavelengths generally shows evidence for either wind-wind collisions in binary systems or magnetic confinement of the wind. In the next four subsections, we summarize some of these theoretical and observational studies.

1.2. Colliding Wind Shocks

In binary systems where both stars have strong winds, shock heating in the wind interaction zone between the two stars can lead to stronger X-ray emission than that seen in the EWS scenario (Stevens et al. 1992; Pittard 2009). The X-ray properties of CWS sources depend on the wind and orbital parameters of the two stars, and they vary with orbital phase in the case of systems with eccentric orbits. Antokhin et al. (2004) predict that X-ray luminosity scales as the reciprocal of the binary separation. In many O+O, WR+O, and LBV+O-type systems in which both components have high mass-loss rates, CWS X-rays tend to dominate those from embedded wind shocks, with X-ray flux increasing for more equal-momentum winds and intermediate separations.

For example, the O+O binaries in the *XMM-Newton* survey of hot stars (Nazé 2009) have, on average, ~ 3 times higher L_X/L_{bol} than single O stars. We note that most single and binary O stars in the *XMM* survey show relatively low-temperature shocks. In fact, the only O+O binaries in the *XMM* surveys with hard X-ray spectra are the long-period

Carina binaries HD 93403, O5 III(fc) + O7 V (Nazé 2009), and HD 93343, O8 V + O7-8.5 V (Antokhin et al. 2008). Long-period, WR+O and LBV+O binaries like WR 140 and η Car also show very high-temperature shocks (Pollock et al. 2005; Corcoran et al. 2001).

Pittard (2009) model the colliding wind emission from pairs of O6 V + O6 V stars with varying orbital periods; their simulations predict peak temperatures of 3-4 MK and 10-20 MK for models CWB1 (3-d period) and CWB2 (10-d period), respectively. We will examine these issues in more detail in §6.3.

It can sometimes be difficult to confirm the binary nature of systems with X-ray properties indicative of CWS emission. Spectroscopic or photometric orbital variations are difficult to measure when the orbital inclination is low, although persistent observing (Hoffmeister et al. 2008) and complementary approaches (Nelán et al. 2004) reveal long-suspected companions in CWS systems. After many years of monitoring, Gamen et al. (2008) derived a 207.7-d orbital period for the Carina WN6h colliding-wind binary WR 25. Observations of non-thermal radio emission often provide clues about the presence of wind-wind interactions in binaries, even when binary orbital parameters cannot be measured (Dougherty & Williams 2000; De Becker 2007). Ideally, X-ray monitoring over multiple orbital periods is needed to show the orbital modulation expected from colliding wind systems, at least those with sufficiently high eccentricities.

1.3. Magnetically Confined Wind Shocks

Where strong, large-scale magnetic fields exist on early-type stars, wind streams from opposite hemispheres are channeled toward the magnetic equator, where they collide head-on, leading to strong shocks and associated X-rays (Babel & Montmerle 1997). MCWS X-ray emission can be differentiated from EWS X-rays by its temperature distributions (Wojdowski & Schulz 2005), which can be dominated by plasma with temperatures of 30-50 million K. For oblique dipole configurations, the X-rays can be rotationally modulated due to differential occultation of the shock-heated plasma by the star (Gagne et al. 1997).

The prototype MCWS source is θ^1 Orionis C, O7 Vp, the illuminating star of the Orion Nebula, which has a 1.5 kG oblique dipole field, measured with Zeeman spectropolarimetry (Donati et al. 2002; Wade et al. 2006). *Chandra* grating spectroscopy shows a high X-ray luminosity (corresponding to $L_X > 10^{-6}L_{\text{bol}}$) and peak X-ray emission measure ~ 33 MK. The X-rays vary (by roughly 20%) in a manner consistent with the rotationally modulated magnetic field configuration, and these X-ray properties are well explained by MHD simulations of the confined wind of this star (Gagné et al. 2005).

Early B stars of the chemically peculiar B2p class show very strong dipole magnetic fields, though they have much weaker winds than the O star θ^1 Ori C. Some, like the prototype σ Ori E, have modest, relatively hard X-ray emission (Sanz-Forcada et al. 2004; Skinner et al. 2008), while other B2p stars have no X-ray emission or emission at levels below the detection threshold. Even the stronger X-ray sources among these Bp stars have X-ray luminosities of only $L_X \approx 10^{30}$ ergs s $^{-1}$ cm $^{-2}$ (Drake et al. 1994).

The ability to channel a wind depends both on the strength of the magnetic field and (inversely) on the density of the wind. These scalings are verified in detail by MHD simulations (ud-Doula & Owocki 2002; Gagné et al. 2005). Some O stars with strong winds and weak fields, such as ζ Ori, have X-ray emission consistent with the EWS scenario (Cohen et al. 2006).

On the other hand, the other well-studied magnetic O stars such as HD 108, O7 Ifpe, and HD 191612, O6.5 IIIf, have $L_X/L_{\text{bol}} \approx -6.2$ and $kT \approx 0.3$ keV. They are more X-ray active than typical EWS sources, but substantially cooler than θ^1 Ori C (Donati et al. 2006a; Nazé et al. 2007, 2010). Also curious is the early B star, τ Scorpii, B0.2 V, which has a highly structured (non-dipole) field (Donati et al. 2006b), strong and hard X-ray emission, but no evidence for wind confinement of the X-ray emitting plasma (Cohen et al. 2003; Ignace et al. 2010).

At this point, there are too few O and early B stars with well-characterized magnetic fields (aside from several dozen Bp stars), and their X-ray properties are too heterogeneous, to make definitive statements about what X-ray signatures will be seen from magnetic OB stars in Carina. However, we can say that it is possible that strong X-ray emission may be produced in Carina O stars via magnetically confined shocks if conditions are right. Overall, though, the general X-ray properties from the MCWS mechanism – elevated X-ray luminosities, hard X-ray spectra, and time variability – overlap with those from the CWS mechanism, though the variability in CWS systems is orbital, whereas the variability in MCWS is often rotationally modulated.

1.4. Unseen Pre–Main-Sequence Companions

The three X-ray emission mechanisms described above convert the kinetic energy of the supersonic wind into shocks and thermal X-ray emission. As the mass-loss rate and terminal wind speed diminish towards later spectral type, embedded wind shocks, colliding wind shocks, and magnetically confined wind shocks should be much weaker.

In star-forming regions, at spectral subtype \sim B2, L_X falls below a few 10^{30} ergs s $^{-1}$

(Caillault et al. 1994; Daniel et al. 2002), and the upper end of the low-mass PMS X-ray luminosity function begins to outshine the massive stars. It is now generally understood that hard, variable X-ray emission from main-sequence mid-B to late-A type stars is produced by unseen, lower-mass companions (Gagné et al. 1995; Briggs & Pye 2003). In most cases, the X-rays provide the only clue to the presence of cool companions. In a reverse application, Evans et al. (2011) use X-ray detections in the CCCP and BV photometry to identify unknown B stars in Tr 16.

The situation for the PMS intermediate-mass stars, i.e., the Herbig Ae/Be stars, is quite different. Many are copious, often hard X-ray emitters, despite the fact that they have weak winds and radiative outer envelopes, so they are not expected to have wind shocks, or solar-type magnetic activity. Skinner et al. (2004) consider low-mass PMS companions and an intrinsic, rotational shear dynamo to explain the X-rays from Herbig Ae/Be stars, but so far the mechanism is not known.

1.5. Other X-ray Emission Mechanisms

In this paper, we assume that the soft X-ray emission from most O stars is produced in shock-heated, collisionally ionized, thermal plasmas. Specifically, plasmas whose densities are high enough to be modeled by equilibrium ionization codes like APEC.

However, other emission mechanisms have been proposed to explain the X-ray properties of massive stars. Most fundamentally, Pollock (2007) suggests that the X-rays from O supergiants like ζ Orionis, O9.7 Ib, are produced in the far wind where densities are low, and where the Coulomb collisional mean-free path is many stellar radii, so that the shocked wind is far from collisional or thermal equilibrium. In the Pollock (2007) scenario, *ions*, not electrons, ionize ions, and the shocks are collisionless; shock heating occurs via plasma processes and magnetic fields. The major difficulty with the Pollock (2007) paradigm is that the X-ray spectra of O stars appear to be produced by collisionally ionized, thermal plasmas with electron-ion bremsstrahlung continua (c.f., Raassen et al. 2008).

The low-resolution ACIS CCD spectra from the CCCP cannot directly address the fundamental nature of the shock heating; we use the APEC model to estimate plasma temperatures and emission measures because the APEC model fits the CCD spectra well with only a few free parameters. When time variability or high-temperature components are observed, we examine secondary processes like colliding wind shocks, magnetically confined wind shocks, or coronal emission from unseen, lower-mass, pre-main-sequence companions, though other mechanisms have been proposed.

For example, the rigidly rotating magnetosphere model (Townsend & Owocki 2005; Townsend 2008) and its successor, the rigid-field hydrodynamic model Townsend et al. (2007), have been used to model the X-ray, UV and H α emission of the He-strong stars like σ Ori E. This model may have applications to other B stars with strong magnetic fields like τ Sco, B0.2 V.

For the O9.5 V spectroscopic binary θ^2 Ori A, Schulz et al. (2006) proposed an interaction between the magnetospheres of the spectroscopic primary and secondary at periastron to explain its x-ray spectrum and time variability. Magnetic fields have yet to be seen on either component, though.

Cassinelli et al. (2008) proposed a model for OB stars in which the thin fast wind forms bow shocks on dense, slowly moving clumps. The adiabatic shocks produce peak emission measure near $\log T = 6.5$, with some emission out to $\log T = 7.5$. It is unlikely that this model can operate in stars with strong magnetic fields like τ Sco or θ^1 Ori C, but it might be viable in non-magnetic OB stars, though the effects of radiative cooling should be added to test the model further.

Waldron & Cassinelli (2009) proposed a highly accelerated diamagnetic plasmoid model to explain the production of high-temperature plasma very close to the photospheres of some O stars. This is essentially the opposite mechanism proposed by Cassinelli et al. (2008). In the diamagnetic plasmoid model, the blobs are ejected from the surface and plow into the cooler, slowly moving plasma at the base of the wind.

The origin of magnetic fields on massive stars is still not fully known. They could be generated by subsurface convection or via differential rotation, or they could be fossil fields. In the Spruit (2002) dynamo model, and its adaptation by Mullan & MacDonald (2005); Mullan & Waldron (2006), differential rotation and Tayler instabilities in the interior magnetic field lead to surface magnetic fields. Finally, we note that some of the known OB stars in Carina could harbor neutron star companions, producing strong, accretion-driven X-ray emission (e.g., Davidson & Ostriker 1973).

The discovery of magnetic fields on some massive stars, in combination with colliding winds from massive binaries, leads to a number of complicated but intriguing X-ray emission mechanisms. In this paper, we will focus on the X-ray diagnostics – variability, high L_X/L_{col} or high kT – that may signal the presence of magnetic fields or colliding wind shocks in the Carina massive stars.

2. Carina OB Star Optical Catalog

The goal of this study is to characterize the X-ray properties of the O and early-B stars with reliably determined spectral types in the ~ 1 square degree CCCP field, and to correlate those X-ray properties with effective temperature, bolometric luminosity, and binary properties. The optically selected sample is biased towards stars that are bright from 3900–4800 Å, and those that are close to the well-studied clusters Trumpler 14, 15 and 16, Bochum 10 and 11, and Collinder 228. This sample complements the X-ray selected massive-star candidates of Povich et al. (2011a), though these are also biased towards luminous stars because of the correlation between L_X and L_{bol} . The optically selected sample is biased to stars with $A_V < 3$ mag while the candidate massive stars of Povich et al. (2011a) are mostly obscured stars with $A_V > 3$ mag.

We began with the “Catalogue of Stellar Spectral Classifications” (Skiff 2009, and references therein) selecting stars with spectral type O2-B3. To these we added stars in Tapia et al. (2003); Smith (2006); DeGioia-Eastwood et al. (2001); Walborn (1995); Massey & Johnson (1993), including two B5 stars, and a B7 star. For some individual stars, mostly spectroscopic binaries and Ofc stars, we used the updated spectral types of Morgan et al. (1955); Morrison & Conti (1980); Morrell et al. (1988); Rauw et al. (2000, 2001); Freyhammer et al. (2001); Albacete Colombo et al. (2002); Niemela et al. (2006); Rauw et al. (2009); Maíz Apellániz et al. (2010); Walborn et al. (2010); Sota et al. (2011).

The spatial distribution of the 200 OB stars is shown in Figure 1, where the clusters Trumpler 15, 14, and 16 are visible from N to S at $-59^\circ 24'$, $-59^\circ 36'$, and $-59^\circ 42'$, respectively. Many of the confirmed massive stars seen in Fig.1 are coincident with the low-mass populations in the rich clusters (Tr 14, Tr 15, Tr 16, and Coll 228), as expected. However, a significant fraction lie well outside the clusters, supporting the idea that star formation in Carina has been ongoing for a considerable length of time, allowing stars to drift or be ejected from their natal groupings. This is discussed further by Feigelson et al. (2011); Povich et al. (2011a,b).

Johnson UB V photometry was gleaned primarily from the photoelectric catalog of “Homogeneous Means in the UB V System” and its update “UB V Photoelectric Cat: Data 1986-1992” (Mermilliod 1994), and the CCD survey of Trumpler 14 and 16 by Massey & Johnson (1993). For a few close visual binaries, we obtained UB V from Massey et al. (2001); Vazquez et al. (1996); Forte & Orsatti (1981); Forte (1976).

We note that a number of other CCD and photoelectric photometry studies have been published on the Carina hot stars, particularly for those in Trumpler 14 and 16. For example, the compilation of Reed (2005), “Photometry and Spectroscopy for Luminous Stars” lists V ,

$U - B$, and $B - V$ from a number of reliable photometric surveys. Unfortunately, only 101 of the 200 OB stars in the CCCP are listed in the Reed (2005) catalog. Some surveys like DeGioia-Eastwood et al. (2001) and the *Tycho* catalog measured B and V . After analyzing color-magnitude diagrams from a number of these studies, we chose the compilations of Mermilliod (1994) and Massey & Johnson (1993) as our primary references because they provided consistent UB V measurements for all but one star: HD 92937, B2.5 II.

For the 70 O stars, effective temperature was interpolated on the basis of spectral type, using the observational T_{eff} scale of Martins et al. (2005a). For consistency, we used the O-star synthetic colors of Martins & Plez (2006) to estimate $(B - V)_0$ and bolometric correction. We note that the Martins et al. work uses solar abundance, wind- and line-blanketed, non-LTE model atmospheres, that, for OB stars, lead to lower T_{eff} and L_{bol} for a given observed spectral type than did previous work.

For the 130 B stars, consistent sets of NLTE synthetic colors, effective temperatures, and bolometric corrections were not available, though NLTE effects are expected to be smaller in the lower-luminosity Carina B dwarfs. We used the intrinsic colors of Wegner (1994) to estimate $(B - V)_0$. For the B stars, we used the bolometric corrections and effective temperature scale of Bessell et al. (1998).

2.1. Reddening and Bolometric Luminosity

This study and the study of Nazé et al. (2011) rely on two methods for determining L_{bol} : (1) the spectral energy distribution (SED) fitting method of Povich et al. (2011a), and (2) the more traditional method employing color excess and bolometric correction. We recall that in the color excess method, $M_{\text{bol}} = V - A_V - DM + BC_V$, $R = A_V/E(B - V)$ and $E(B - V) = (B - V) - (B - V)_0$, where BC_V is the V -band bolometric correction and DM is the distance modulus.

Of the 200 OB stars in our spectroscopic sample, 182 have high-quality UB V , 2MASS JHK and *Spitzer* IRAC photometry in the VelaCarina Point-Source Archive (PI: S. Majewski, Povich et al. 2011b). Povich et al. (2011a) used the SED fitting method of Robitaille et al. (2007), which applies an ISM absorption model to the revised ATLAS9 stellar atmosphere models of Castelli & Kurucz (2004). Though we recognize that the ATLAS9 LTE model atmospheres do not account for non-LTE wind and line blanketing effects, Povich et al. (2011a) show that LTE and non-LTE atmospheres produce similar broad-band optical/infrared SEDs, and hence very similar estimates of A_V and L_{bol} .

Recognizing that a number of stellar and ISM parameters can adequately fit a 10-point

SED, Povich et al. (2011a) generate a family of solutions for each SED. The 182 OB stars in the validation sample have the advantage of having well-determined spectral types, and hence T_{eff} , thereby significantly reducing the number of statistically acceptable solutions, and significantly constraining A_V and L_{bol} .

The SED fitting depends on the adopted reddening law, which effectively specifies the scaling between A_V and the absorption in each photometric band. In the traditional color excess method, this comes down to choosing $R_V = A_V/E(B - V)$. As described in Povich et al. (2011a), the estimates for R_V in Carina have varied from an ISM value of 3.1 or 3.2 (Turner et al. 1980a; Turner & Moffat 1980b) to above 5.0 (Herbst 1976).

Table 1 of Walborn (1995) illustrates the interplay between R and DM in the Carina clusters. Throughout the CCCP, we adopt DM = 11.81, corresponding to $d = 2.3$ kpc, the distance to η Carinae derived from the Doppler velocity and proper motion of the expanding Homunculus nebula (Smith 2006). Walborn (1995) find that for this distance modulus, $R = 4$ provides the best fit to the O stars in Tr 16, though star-to-star, and cluster-to-cluster variations probably do exist. Similarly, Povich et al. (2011a) find better agreement between the L_{bol} estimates using $B - V$ and those derived from the optical-infrared SED method using $R_V = 4$ than using $R_V = 3.1$ or $R_V = 5$. Hence, we and Povich et al. (2011a) adopt an average $R_V = 4$ and $d = 2.3$ kpc to all the stars in Carina. We do not attempt to account for star-to-star variations in the reddening law.

We note that, based on Walborn’s analysis of six O stars in Tr 14, $R_V = 4$ implies DM = 12.33 if the Tr 14 and Tr 16 are coeval (and thus the O stars in both clusters have the same average luminosity). A more likely solution, however, is that Tr 14 is younger than Tr 16 and the main-sequence O stars are sub-luminous relative to the average class V calibration.

For 181 of the 200 stars in the Carina OB database, we compute L_{bol} using both the SED (tag name LOGLBOL_SED) and color excess (LOGLBOL_BV) methods. We note that one star, MJ 501=Tr 16 74, B1 V, has unreliable $B - V$. For these 181, the offset in A_V (SED - BV) is $\Delta A_V = 0.1$ with a standard deviation $\sigma = 0.25$ mag. This is a lower bound on the systematic uncertainty in A_V . The offset in $\log L_{\text{bol}}$ (SED - BV) is $\Delta \log L_{\text{bol}} = 0.04$ with a standard deviation $\sigma = 0.14$ mag.

We note though that CMFGEN model atmospheres (Hillier & Lanz 2001) produce more EUV, NIR, and MIR emission for a given T_{eff} and $\log g$ than non-LTE model atmospheres, especially for O supergiants. Because we wish to exploit the full set of optical, near- and mid-infrared photometry, and to maintain consistency with the rest of the CCCP, we use the SED-derived L_{bol} values whenever possible, despite this deficiency. Future updates to

the OB catalog will contain new L_{bol} estimates, based on updated SED-fitting codes.

The FITS table headers and the CDS header files list the name, unit, and fortran format code for all columns in the OB catalog. The first 38 columns are devoted to the optical/infrared database and include the following columns (or tags): IAU J2000 name, default designation (label), HD name, CPD name (from the 1919 list of Cannon, Pickering & Draper), LS or ALS name (Reed 2005), Feinstein Trumpler 14/15/16, Collinder 228, or Bochum 10/11 designation, and Massey & Johnson (1993) designations. J2000 R.A. and Decl. are listed in decimal degrees and sexagesimal hours and degrees. Also listed are spectral type, spectral type reference, binary flag, notes, V , $U - B$, $B - V$, Q (Massey & Johnson 1993), and UBV reference. We list the derived quantities $(B - V)_0$, $E(B - V)$, BC, and A_V , $\log L_{\text{bol}}$ (solar units), and $\log T_{\text{eff}}$ as determined via the color excess method, the SED fitting method, and the adopted value. We note that the label tag contains the commonly used designation used in the text, tables and figures, but that the other designations in the electronic files are precisely those used by *Simbad*, and by association other databases, for rapid searching.

Table 1 shows a cross section of the optical database for the most luminous stars, sorted by $\log L_{\text{bol}}$. Figure 2 shows the resulting H-R diagram. We overlay the *average* main sequence of Martins et al. (2005b) from their sample of 1-5 Myr-old stars. The B-star main sequence is from de Jager & Nieuwenhuijzen (1987) (see also Povich et al. 2011a).

The zero-age main sequence (ZAMS) is clearly delineated in Fig. 2, as is the extent of the terminal-age main sequence (TAMS). The supergiants and bright giants are shown with white dots. The uncertainty in L_{bol} is dominated by random photometric errors (0.1 mag) and by systematic uncertainties, especially in the distance modulus and $R = A_V/E(B - V)$, on the order of 0.3 mag. As noted earlier, we use a global reddening law; we do not account for possible star-to-star variations in R . Despite these uncertainties, much of the spread above the ZAMS appears to indicate a real spread in age. We note that the most luminous OB star in Carina, QZ Car, is a quadruple system (Parkin et al. 2011). T_{eff} for the candidate Herbig Be star SS73 24 was estimated from its optical-infrared SED (see §6.4.1).

All but two of the 70 O stars were detected with at least 3 source counts in the CCCP: Tr14-27, O9 V, Tr15-18, O9 I/II:(e:). Tr15-18 also has the highest A_V of all 200 OB stars; it may have avoided detection because of its high column density. While $A_V = 5.66$ mag for Tr15-18 is high among the known OB stars, it is typical of the X-ray selected candidate OB stars identified by Povich et al. (2011a). Finally, we note that Tr15-19, O9 V, and Tr15-21, B0 III, are well below the ZAMS; they may be a background stars, not members of Trumpler 15 (Tr 15).

To estimate the completeness of the optical OB catalog, we consider the populations of OB stars with measured spectral types, and the 94 X-ray-detected stars without measured spectral types discovered by Povich et al. (2011a). Using an initial mass function (IMF) exponent $\Gamma = -1.3$ (Kroupa 2002), normalized to the 47 LBV, WR, and O2-O8.5 V stars with mass $M > 20M_{\odot}$, we expect to find 24 stars in the mass range $15 - 20M_{\odot}$, compared to 27 O9 and O9.5 stars, and 130 stars in the mass range $7 - 15M_{\odot}$, compared to 123 main-sequence B0-B2.5 stars. Note, we are considering only the primary stars. This suggests that, if the number of early-mid O stars is complete, then the number of late-O and early-B stars is also nearly complete.

However, the 94 stars identified by Povich et al. (2011a) with $L_{\text{bol}} > 10^4 L_{\odot}$ could have main-sequence spectral types as early as O4. I.e., the Povich et al. (2011a) result implies that a substantial fraction of early-O to early-B stars do not have measured spectral types. To estimate this fraction more precisely, we note that 140 stars in our optical catalog have $L_{\text{bol}} > 10^4 L_{\odot}$, and that 76% are detected in the CCCP. Applying this detection fraction to the 94 stars in Table 3 of Povich et al. (2011a) suggests approximately 124 stars with $L_{\text{bol}} > 10^4 L_{\odot}$. I.e., an additional ~ 30 luminous stars were not detected with *Chandra*. This suggests a total population of $140 + 94 + 30 = 264$ luminous stars; our optical catalog is thus $\sim 53\%$ complete.

Thus if the Povich et al. (2011a) result is confirmed, then a significant fraction (up to half) of the OB stars in the CCCP region have yet to be spectroscopically identified. These stars have higher than average A_V and generally reside outside the well-studied clusters in Carina. Similarly, Wright et al. (2010) find that a large fraction of the B-star population in the Cyg OB2 star-forming region is not identified.

3. Carina OB Star X-ray catalog

The 200 OB star optical positions were matched to the list of 14368 CCCP sources (see Broos et al. 2011a, for a detailed description of the catalog matching). The astrometric systems in the two catalogs were well aligned ($\Delta\alpha = 0.005''$ and $\Delta\delta = 0.012''$), and the optical and X-ray positions reported for individual stars were in good agreement (the median offset was $r \approx 0.19''$). This initial pass through the CCCP X-ray data produced 118 matches (out of 200), including 67 of 70 O stars, and 51 of 130 B stars.

In order to estimate count upper limits for the 82 OB stars not detected in the automated *ACIS Extract* procedure described by Broos et al. (2011a), we determined optimal source and background regions for the undetected OB stars at their optical positions, accounting

for the *Chandra* point spread function and the presence of nearby X-ray point sources.

The full *ACIS Extract* procedure was run again on the combined list of 14 368 sources, 82 undetected OB stars, and a number of photometrically selected candidate mid-to-late B stars (Evans et al. 2011). The *ACIS Extract* procedure used in the CCCP produces source, background and net counts in three bands: hard (2-8 keV), soft (0.5-2 keV) and total (0.5-8 keV). The procedure also estimates the probability P_B in these three bands that the source counts were produced by fluctuations in the observed local background.

Although they were not identified in the automated source detection procedure, an additional 11 stars met the detection criteria used in the CCCP catalog: at least 3 extracted counts and $P_B \leq 0.01$ in a least one of the three bands (Broos et al. 2011a). They are: Coll228-66, O9.5 V, LS 1745, B2 III, HD 305515, B1.5 Vsn., Tr16-13, B1 V, HD 305534, B0.5 V: + B1 V:, Tr16-29, B2 V, LS 1866, B2 V, Tr16-33, B2 V, HD 93342, B1 Iab-Ib, Coll228-81, B0.5 V, HD 93723, B3 III. Thus, the only undetected O stars are Tr14-27, O9 V, Tr15-18, O9 I/II:(e:). Thus the OB catalog contains 129 X-ray matches (out of 200), including 68 of 70 O stars, and 61 of 127 B0-B3 stars. We note that the three stars with spectral types later than B3 were not detected in X-rays.

For the undetected stars, the 90% count rate upper limit, NETCOUNTS_HI_T is used to derive a photon flux upper limit corrected for the mean effective area in the 0.5-8 keV band, the effective exposure time, and the PSF fraction of the selected source extraction region (using eqn. 1 in Broos et al. 2011a).

The 200 OB stars have been divided into three groups: (1) 63 undetected stars with $P_B > 0.01$ for which we calculate a photon flux upper limit, (2) an additional 51 X-ray detected OB stars with 3-50 counts, for which we also determine median energy, $E_{\text{med}} = \text{MEDIANENERGY_T}$ and the 0.5-8 keV absorbed (uncorrected) energy flux, $f_X = \text{ENERGYFLUX_T}$ (see eqns. 1 and 2, Broos et al. 2011a), and (3) 78 stars with at least 50 net counts for which Nazé et al. (2011) also derive kT and N_H by fitting the ACIS spectra in XSPEC with a one- or two-temperature VAPEC emission model, and a two-component TBABS absorption model.

The results of the XSPEC fitting procedure are described fully by Nazé et al. (2011), but the absorption modeling deserves mention here. For all 200 OB stars, we have estimated A_V and converted that absorption into an ISM column density using $N_H/A_V = 1.6 \times 10^{21} \text{ cm}^2 \text{ mag}^{-1}$ (Vuong et al. 2003; Getman et al. 2005)¹.

In the XSPEC fits, Nazé et al. (2011) fix the first ISM column density parameter, and

¹We note that the N_H/A_V ratio is robust to very high A_V , but that the scatter in the N_H versus A_V diagram is quite large, especially at high A_V .

allow a second column density parameter to vary. Many OB-star CCD spectra appear to require this extra absorption, presumably caused by absorption of shocked emission in the overlying wind.

The absorbed X-ray fluxes, used in this paper were computed in XSPEC with the first absorption parameter set to $N_{\text{H}}^{\text{ISM}}$, and the second absorption parameter at its best-fit value. The *unabsorbed* fluxes were computed using the best-fit emission model, the ISM absorption parameter set to zero, and the second absorption parameter at its best-fit value. This way the unabsorbed flux represents the flux emerging from the far-wind of the star, corrected for ISM absorption. L_{X} is the corresponding 0.5-8 keV unabsorbed X-ray luminosity assuming $d = 2.3$ kpc, FITLUMINOSITY_TC.

We note that Nazé et al. (2011) derive the absorption-corrected 0.5-10 keV X-ray luminosity, related to tag name FCTO, assuming the same distance. We note that 0.5-8.0 keV is the total band of the CCCP, and 0.5-10 keV is the default energy range of previous *XMM-Newton* surveys (e.g., Sana et al. 2006b). The two X-ray luminosities are very similar, with an average offset of 0.008 in the log, and RMS deviation of 0.033 in the log.

We note that the four X-ray brightest stars were piled up in the CCCP ACIS-I data: HD 93129A, O2 If*, HD 93205, O3 V + O8 V, HD 93250, O4 III(fc), and QZ Car, O9.7 I + O8 III. A more extensive set of QZ Car data have been fully analyzed by Parkin et al. (2011). In the X-ray catalog, we use the average QZ Car parameters in Table 4 of Parkin et al. (2011). For HD 93129A and HD 93205 Nazé et al. (2011) performed their two-temperature XSPEC analysis on the pileup-corrected spectrum (for more details see Broos et al. 2011a). For HD 93250, we used a series of *Chandra* ACIS-S observations; these data and the XSPEC spectral analysis are described in Appendix A.

Throughout this paper, we use kT_{avg} , the emission-measure weighted mean kT for the 78 OB stars with XSPEC fit parameters. For the 53 stars with one-temperature XSPEC fits, $kT_{\text{avg}} = kT_1$. For the 24 stars with two-temperature XSPEC fits, and for QZ Car’s three-temperature fit, $kT_{\text{avg}} = \Sigma kT_i n_i / \Sigma n_i$, where n_i is the normalization parameter of the i th temperature component. The volume emission measure is $4\pi d^2 \Sigma n_i$.

Thus, in addition to the many parameters produced by the extended *ACIS Extract* procedures described by Broos et al. (2011a), our OB X-ray database contains an additional 30 parameters to describe the results of the two-temperature XSPEC fits of Nazé et al. (2011). Merging the X-ray parameters with the optical parameters for each star produces a set of tables with 200 rows (one row for each OB star). We used the following column names (i.e., IDL structure tags) extensively to create the figures and tables in this paper: LABEL, SPTYPE, KTMEAN, LOGLBOL, LOGT, PROBKS_SINGLE, PROBKS_MERGE,

PROBNOSRC_T, NETCOUNTS_T, NETCOUNTS_HI_T, FITLUMINOSITY_TC, MEDIANENERGY_T, ENERGYFLUX_T, where _T refers to the total 0.5-8 keV band, and _TC refers to total band, absorption-corrected.

The full set of optical/X-ray tables are available electronically as a machine-readable tables from the CDS, a FITS binary table file, and an IDL save file². The catalog can also be queried from the Vizier database at the CDS.

4. X-ray Spectral Results

Tables 2 and 3 summarize the X-ray properties for the single O stars and the known O+O binaries, respectively, sorted by $\log L_X/L_{\text{bol}}$. Table 4 summarizes the X-ray spectral and timing analysis results for the 28 X-ray brightest B stars, sorted by $\log f_X$. From Tables 2, 3, and 4 we find:

1. The great majority of single and binary O stars have $-6.8 < \log L_X/L_{\text{bol}} < -8.0$ and have soft X-ray spectra characterized by $kT_{\text{avg}} < 0.8$ keV.
2. A small number of single O stars have hard X-ray spectra characterized by $kT_{\text{avg}} \gtrsim 1$ keV: HD 93250, O4 III(fc), MJ 496, O8.5 V, and MJ 449 = LS 1865, O8.5 V((f)).
3. The spectroscopic O+O binaries with $P_{\text{orb}} > 10$ days like QZ Car, HD 93403 and HD 93343 show hard X-ray spectra characterized by $kT_{\text{avg}} > 1$ keV.
4. The O+O binaries with $P_{\text{orb}} < 10$ days like HD 93205, HD 93161A, FO 15 and five other known short-period O+O binaries in Tr16 have softer X-ray spectra characterized by $kT_{\text{avg}} < 1$ keV.
5. The shortest-period binary in Carina, FO15, O5.5 Vz + O9.5 V, has low $\log L_X/L_{\text{bol}} \approx -7.65$.
6. All but one of the B stars with $\log L_X \gtrsim 31$ have $kT_{\text{avg}} \gtrsim 1$ keV
7. All but one of the B stars with $\log L_X < 31$ or $\log f_X < -14$ have relatively soft X-ray spectra, with $kT_{\text{avg}} < 0.6$ keV.

²The FITS and IDL save files are available from the authors upon request.

The L_X/L_{bol} patterns have been discussed in detail by Nazé et al. (2011). We recall that the ISM-corrected L_X is computed for the 78 stars with more than 50 counts in XSPEC, whereas f_X , which is not corrected for ISM absorption, was computed for all the X-ray detected stars in *ACIS Extract* (except HD 93250, HD 93129A, HD 93403 and QZ Car). Noting that $f_{\text{bol}} = L_{\text{bol}}/4\pi d^2$, in Figure 3 we show $\log f_X$ versus $\log f_{\text{bol}}$ using the same symbol definitions as Figs. 1 and 2 to highlight the location of early and late, single and binary O stars, B stars, and hard and soft X-ray spectra.

In Figs. 3 and 4, the 51 X-ray detected stars with 3-50 counts are shown as filled diamonds; 49 are B stars (pink). We categorize the OB stars as *hard* (with $kT_{\text{avg}} > 1.8$ keV, shown as triangles in scatter plots), *medium-energy* (with kT_{avg} in the range 1-1.8 keV, squares), and *soft* (with $kT_{\text{avg}} < 1$ keV, circles). In Figs. 3 and 4a, the upper dotted lines represent $\log f_X/f_{\text{bol}} = -7$ and the lower dashed lines represent $\log L_X/L_{\text{bol}} = -7.23$, the mean of $\log L_X/L_{\text{bol}}$ with $kT_{\text{avg}} < 1$ keV.

The upper and lower panels of Figure 5 show the number distributions of $\log L_X$ and $\log f_X$, respectively, for O and B stars: early-O binaries are black, early-O single stars are blue, late-O binaries are dark green, late-O single stars are light green, and B stars are pink.

Fig. 3 shows two populations of O stars (green and blue/black symbols): (i) a population of relatively cool X-ray sources clustered around $\log f_X/f_{\text{bol}} \approx 7.55$, though there are some hotter sources in this group, and (ii) a group of sometimes hotter X-ray sources with higher $\log f_X/f_{\text{bol}}$. This trend is emphasized in Figure 4, which plots $\log L_X/L_{\text{bol}}$ versus kT_{avg} and $\log f_X/f_{\text{bol}}$ versus median energy E_{med} for the same samples as Fig. 3. The dotted and dashed vertical lines coincide with the dividing lines between soft, medium and hard symbol definitions used in Figs. 1-4. The soft, low L_X/L_{bol} stars are clumped in the lower left of both panels of Fig. 4. The horizontal dotted and dashed lines correspond to $\log L_X/L_{\text{bol}} = -7$ and -7.23 . This latter value is the mean of $\log L_X/L_{\text{bol}}$ for the stars with $kT_{\text{avg}} < 1$ keV (Nazé et al. 2011).

The upper and lower panels of Figure 5 show the distributions of $\log L_X$ and $\log f_X$, respectively, for the samples shown in Figs. 3 and 4. The upper and lower panels of Figure 6 show the distributions of $\log L_X/L_{\text{bol}}$ and $\log f_X/f_{\text{bol}}$, respectively, for the samples shown in Figs. 3-5. The histograms suggest two distributions, as do Figs. 3 and 4: a group of stars centered around $\log L_X/L_{\text{bol}} < -6.8$ and $kT_{\text{avg}} < 1$ keV, and a group with somewhat higher $\log L_X/L_{\text{bol}}$ and $kT_{\text{avg}} \geq 1$ keV. We note a similar pattern for the B stars.

The upper and lower panels of Figure 7 show the distributions of kT_{avg} and median energy E_{med} , respectively, for the samples in Figs. 3-6. The upper panel of Fig. 7 reflects the trend seen in the top panel of Fig. 4: a large distribution of OB stars with $kT \approx 0.5$ keV,

and a small, broad distribution of stars with $kT > 1$ keV. The lower panel of Fig. 7 shows no clear segregation; E_{med} is a less useful measure of intrinsic X-ray temperature, because higher absorption also produces higher median energy.

Figs. 3, 4, 6 and 7a suggest two populations of OB stars. The first is a low activity group with $\log L_X/L_{\text{bol}} < -6.8$ and $kT < 1$ keV. We suggest that for most of these stars, conventional embedded wind shocks produce most of the X-ray emission. We suggest that the stars with $kT_{\text{avg}} > 1$ keV require an additional X-ray emission mechanism to produce the enhanced activity and hotter X-ray shocks. We will explore these results in more detail for single O stars, astrometric binaries, O+O binaries, and B stars in §6 and §7 below.

Table 4 lists the names, spectral types, and selected X-ray properties of the 28 X-ray brightest early-B stars, sorted by f_X . We note that 14 of the 15 X-ray brightest early-B stars in Table 4 have $\log L_X/L_{\text{bol}} > -7$, that 14 of those 15 have $kT_{\text{avg}} \gtrsim 1$ keV, and that 7 of the top 12 are probably variable on long time scales, though none show the characteristic rapid rise and slower decay of strong PMS flares (see Figs. 9 and 10). For the B stars (in pink), Fig. 4b shows a wide range of median energy and f_X/f_{bol} , with only a slight positive correlation.

We address the origin of the X-ray emission among the 130 early B stars by comparing the X-ray flux distributions of the early B stars and the X-ray detected low-mass stars. Figure 8 shows histograms of log photon flux for 61 X-ray detected early B stars (in pink), 69 B-star upper limits (in brown), and the 14 250 CCCP sources not associated with massive stars (in gray hatching). The vast majority of the general CCCP source population is associated with low-mass PMS stars (Feigelson et al. 2011). The PMS histogram has been normalized to the 130 B stars for comparison. We note that f_X cannot be computed for the undetected sources, so we plot the 0.5-8 keV photon flux (or the 90% confidence upper limit), corrected for the time-averaged PSF fraction and effective area at the location of each star.

At first glance, Fig. 8 suggests that, overall, the X-ray detected B stars have higher flux than the X-ray detected low-mass PMS stars. For example, the 61 X-ray detected B stars have mean X-ray flux $f_X = 4.6 \times 10^{-15}$ ergs cm^{-2} s^{-1} , with a standard deviation $\sigma = 2.7 \times 10^{-15}$ ergs cm^{-2} s^{-1} . The upper limits span one order of magnitude in photon flux, illustrating the non-spatial uniformity of the CCCP survey (c.f. Townsley et al. 2011a). Fig. 8 suggests that the CCCP is only complete to a photon flux of $\sim 10^{-3}$ counts ks^{-1} cm^{-2} .

Adjusting for this bias, two results emerge from Fig. 8: (i) the B stars with log photon flux below -2.3 , corresponding to $\log f_X < -14$ ergs cm^{-2} s^{-1} , appear to have the same flux distribution as the low-mass PMS stars, with a companion fraction $\sim 50\%$, and (ii) the

distribution of B stars with $\log f_X > -14$ ergs $\text{cm}^{-2} \text{s}^{-1}$ cannot be explained by a distribution of typical, low-mass PMS companions.

Result (i) is consistent with the results of Evans et al. (2011): most X-ray detected B stars probably harbor coronal PMS companions. Result (ii) suggests either (1) the brightest dozen or so B stars formed with hyperactive companions, or (2) that their X-rays are produced by some intrinsic shock mechanism.

These stars are: SS73 24, Be pec, Tr16-64, B1.5 Vb, Tr16-10, B0 V, Tr16-5, B1 V, Tr14-28, B2 V, HD 93501, B1.5 III:, Coll228-68, B1 Vn, Tr14-124, B1 V, HD 93190, B0 IV:ep, Tr14-18, B1.5 V, LS 1813, B2 V, Tr16-11, B1.5 V, Tr14-19, B1 V, and Tr14-29, B1.5 V.

5. X-ray Timing Analysis

We have looked for time variability in the CCCP event data of the 129 X-ray detected OB stars in three ways: (1) we visually examined the sequenced and stacked corrected photon flux light curves, (2) we used the merged Kolmogorov-Smirnov test probability, $P_{KS} = \text{PROBK_MERGE}$ in the CCCP data products (Broos et al. 2010), and (3) we used a maximum likelihood procedure to divide the event data into blocks of approximately constant count rate. The latter, an IDL procedure `MLB_ACIS` developed by E. Flaccomio, was used by Wolk et al. (2005) to identify flares in the *Chandra* Orion Ultradeep Project (COUP). An X-ray source is variable if an event list produces more than one maximum likelihood block. In `MLB_ACIS`, the significance thresholds are calibrated as a function of counts using a large set of simulated constant count rate sources. For each star, the number of maximum likelihood blocks, assuming at least 5 counts per block, and 95% confidence, are listed in the last column of Tables 2, 3, and 4.

We note that the maximum likelihood procedure can find two maximum likelihood blocks for a constant source, if that source is observed in two OBSIDs at significantly different off-axis angles. This was not an issue in the study of Wolk et al. (2005) because the COUP observations were all centered on the Trapezium cluster – stars appeared at the same off-axis angle. We note that the photon flux curves produced by *ACIS Extract* are corrected for effective area and do not suffer this bias.

The sequenced photon flux light curves of the visually identified sources are shown in Figures 9 and 10. Some very bright sources like HD 93403 in the lower left panel of Fig. 9, show significant long- and short-term variability, and others like FO 15 in the upper left panel of Fig. 9 show clear long-term variability. None of the OB stars showed the characteristic rapid rise and slower decay of strong coronal flares (Wolk et al. 2005).

6. Notes on Individual Massive Star Systems

In this section we examine the X-ray, optical, infrared, and radio properties of the most X-ray luminous OB stars, dividing them into four categories based on spectral type and binary separation: astrometric O binaries, spectroscopic O+O binaries, apparently single O stars, including weak-wind stars, and B stars.

6.1. Single O-type Stars

Table 2 and Fig. 4 suggest that most single O stars have low L_X/L_{bol} and low kT . Below we consider the three single O stars with $\log L_X/L_{\text{bol}} > -7$ and $kT > 1$ keV: HD 93250, MJ 496 = Tr16-22, and MJ 449 = LS 1865.

6.1.1. HD 93250, O4 III(fc)

The most X-ray luminous O star in Carina, and possibly the most enigmatic, is the Ofc star HD 93250, located east of Tr 14, and north of Tr 16. Though long classified as O3.5 V((f+)) (Walborn et al. 2002; Skiff 2009), Walborn et al. (2010) have reclassified it as O4 III(fc). They write, “The Ofc category consists of normal spectra with C III $\lambda\lambda 4647$ -4650-4652 emission lines of comparable intensity to those of the Of defining lines N III $\lambda\lambda 4634$ -4640-4642.”

HD 93250 was observed far off-axis in a series of HETG/ACIS-S observations of η Car (see Appendix A). The merged ACIS-S spectrum in Figure 11 shows strong Si XIII and Si XIV emission lines and strong Fe K α emission at 6.7 keV, mostly from Fe XXV, confirming the presence of extremely hot plasma ranging in temperature from 6-40 MK. Its mean 0.5-8 keV X-ray luminosity is $L_X \approx 1.5 \times 10^{33}$ ergs s $^{-1}$, similar to the value found by Sanchawala et al. (2007).

Figure 12 shows the L_X light curve of HD 93250 based on the XSPEC fits to the individual ACIS-I and ACIS-S datasets. In all but one OBSID, its X-ray luminosity is marginally consistent with a single value, $L_X \approx 1.45 \times 10^{33}$ ergs s $^{-1}$. During the ACIS-I OBSID 4495 when the source was marginally piled up, $L_X = 1.7 \pm 0.1 \times 10^{33}$ ergs s $^{-1}$, suggesting $\sim 20\%$ time variability on time scales of months (between observations), not unlike the variability seen in a series of 21 *XMM-Newton* spectra of HD 93250 (Rauw et al. 2009).

Based on the spectral fits presented in Appendix A, we use the wind mass column to

derive a mass-loss rate $\dot{M} = 1.4 \pm 0.5 \times 10^{-6} M_{\odot} \text{ yr}^{-1}$. This is a factor of 3-4 smaller than the value estimated by Puls et al. (1996), who did not allow for wind clumping, yet somewhat larger than the recent estimate of Martins et al. (2005b), $\dot{M} = 6 \pm 2 \times 10^{-7} M_{\odot} \text{ yr}^{-1}$.

Oskinova et al. (2007) have shown that the conventional treatment of wind clumping commonly used in stellar atmosphere codes (e.g., Martins et al. 2005b) leads to an underestimate of empirical mass-loss rates by a factor of few. The mass-loss rate for HD 93250 derived from the CCCP spectral fits appears to be generally consistent with the findings of Oskinova et al. (2007).

Along with HD 93129A, HD 93250 is one of only two non-thermal radio O stars in Carina, and De Becker (2007) list it as a “suspected binary” on the basis of its X-ray and non-thermal radio emission. Rauw et al. (2009) note however that the only radio detection of HD 93250 is at 8.6 GHz (Leitherer et al. 1995). The radio flux is assumed to be non-thermal because, if it were thermal, the 8.6 GHz flux would suggest a mass-loss rate $\dot{M} > 10^{-5} M_{\odot} \text{ yr}^{-1}$.

Though HD 93250 shows all the signatures of a colliding wind binary, an optical companion has yet to be detected. Nelan et al. (2004, and Nelan & Walborn 2010, private communication) found no evidence of a luminous astrometric companion in their *HST* FGS data, and Rauw et al. (2009) detected no statistically significant radial velocity variations ($\sigma = 1.3 \text{ km s}^{-1}$ using seven absorption lines over six epochs).

As Rauw et al. (2009) point out, we are left with two plausible scenarios: (i) a wide, massive binary that has evaded detection, or (ii) magnetically confined wind shocks around a single magnetic O4 star.

Magnetically confined wind shocks are difficult to reconcile with strong non-thermal radio emission. Though non-thermal radio emission would be produced in magnetized wind shocks, most of that emission would occur within a few stellar radii of the visible photosphere, well inside the radio photosphere. At 8.6 GHz, the wind of the O4 giant is optically thick out to hundreds of stellar radii (e.g., De Becker et al. 2004).

Given the similarity between the primary of HD 93403, O5 III(fc), and HD 93250, O4 III(fc), in both its optical and X-ray spectral properties, and given the observed correlation between shock temperature and binary period (see Fig. 13 and §6.3), we speculate that HD 93250 is a wide binary with an orbital period of 30-60 days. If the primary also possesses a strong magnetic field, high-S/N X-ray grating spectra will be needed to untangle the origin of the strong X-ray shocks.

Detections at two or more radio frequencies are needed to measure HD 93250’s spectral

index, and to confirm its non-thermal radio emission. In addition, spectro-polarimetric monitoring is needed to look for surface magnetic fields and measure the primary’s rotation period. Ground-based optical interferometry (e.g., Patience et al. 2008) is needed to look for a luminous companion inside the ~ 20 AU limit imposed by the *HST* FGS.

6.1.2. *Tr16-22 = MJ 496, O8.5 V*

The single O8.5 V dwarf MJ 496=Tr 16 22 was detected with *Chandra* by Albacete-Colombo et al. (2008) and Sanchawala et al. (2007) and with *XMM-Newton* by Nazé (2009) and Antokhin et al. (2008). Morrell et al. (2001) use Tr16-22 as a spectroscopic template for the O8 V secondary in the colliding wind binary HD 93205. Compared to the results in Table 3, Albacete-Colombo et al. (2008) derive similar, though slightly lower, kT_1 , kT_2 , L_X , and L_{bol} , and list Tr16-22 as a probable binary. Similarly, Evans et al. (2003) single out Tr16-22 as a possible colliding wind binary. We note however that Tr16-22’s L_X and $\log L_X/L_{\text{bol}}$ are higher than those of any late-O + late-O binary in Carina. As such, Tr16-22 is a good candidate for magnetically confined wind shocks. High-S/N spectro-polarimetric monitoring are needed to detect and measure its magnetic geometry.

6.1.3. *MJ 449 = CPD-59 2610 = LS 1865, O8.5 V((f))*

The last of the apparently single O stars with very hot X-ray shocks is MJ 449 = LS 1865, O8.5 V((f)). We find $\log L_X = 31.42 \pm 0.20$, $\log L_X/L_{\text{bol}} = -6.90$, $kT_1 = 0.59_{-0.3}^{+0.1}$, and $kT_2 > 3.1$ keV, with comparable emission measure in the two thermal components (Nazé et al. 2011). Though MJ 449 is not shown in Fig. 10, it is most likely time variable, with $P_{\text{KS}} = 16\%$, and three maximum likelihood blocks. Like Tr16-22, MJ 449 is a candidate for magnetically confined wind shocks, though its lower $\log L_X/L_{\text{bol}}$ suggests that other emission mechanisms may be at work, including coronal emission from a PMS companion.

6.2. Astrometric Binaries

We first examine the orbital properties and radio emission of the four astrometric binaries detected with *HST*. Nelan et al. (2004) used a series of *HST* Fine Guidance Sensor observations (in high angular resolution mode 1r) to look for luminous companions around O and early B stars in Tr 14 and 16. The observations were typically sensitive to binary separations as low as ~ 10 mas, or ~ 23 AU at $d = 2.3$ kpc. We consider the four O stars

in Table 1 of Nelan et al. (2010). We note that Tr16-31=MJ 484, B0.5 V is a wide binary with a separation of 352 ± 2 mas (~ 810 AU); it is not detected in the CCCP.

6.2.1. HD 93129A, O2 If*

HD 93129A is the earliest O star in Carina, and one of the earliest known in the Galaxy. The O3.5 V((f)) star HD 93129B is located $2.74''$ to the southeast (6300 AU at the distance of Carina) – HD 93129A and B are clearly resolved in the *Chandra* data. Nelan et al. (2004, 2010) discovered a luminous companion, HD 93129Ab, at a separation of $0.053'' \pm 0.003''$ (≈ 122 AU at 2.3 kpc), and $\Delta V = 0.9 \pm 0.05$ mag. Nelan et al. (2004) estimate the primary’s mass to be $M_{\text{Aa}} \approx 110M_{\odot}$, and the secondary’s mass to be $M_{\text{Ab}} \approx 70M_{\odot}$, implying an approximate spectral type o3.5 v for Ab, very similar to HD 93129B. An unpublished analysis by Maiz Apellaniz (2007) indicates that the Aa/Ab system may be approaching periastron in ~ 2020 .

HD 93129A is a strong non-thermal radio source (Benaglia et al. 2006). Benaglia et al. (2010) resolve the emission at 2.37 GHz into what appears to be a bow shock structure, consistent with a wind collision zone at the interface of Aa and Ab. Wide, massive binaries like HD 93129A are sometimes strong non-thermal radio sources because the wind collision zone is outside the radio photosphere of both stars (c.f., De Becker 2007).

Although hard X-ray emission and non-thermal radio emission are usually associated with colliding wind shocks in WR+O binaries, the *Chandra* ACIS-I data do not allow us to establish the location of the X-ray shocks within the HD 93129A system. We note that the system’s $\log L_X/L_{\text{bol}} = -6.85$ is higher than typical single, early-O stars in Table 2, and the spectrum requires a 1.9 keV emission component with about 12% of the total emission measure.

A *Chandra* high-energy transmission grating spectrum of HD 93129A shows broad, asymmetric line profiles, and moderately weak He-like forbidden lines of Si XIII and Mg XI that suggest that most of the X-rays are produced in wind shocks a few R_{\star} from the photosphere (Cohen et al. 2010). The most likely explanation for HD 93129A’s X-ray and radio properties is that both mechanisms are operating: embedded wind shocks close to Aa and Ab, and colliding wind shocks between Aa and Ab.

6.2.2. HD 303308, O4.5 V((fc))

HD 303308 is the fifth most X-ray luminous O binary in Carina with a soft spectrum ($kT \approx 0.25$ keV) and $\log L_X/L_{\text{bol}} \approx -6.89$. Nelan et al. (2010) find a binary separation of 15 ± 2 mas, corresponding to ~ 35 AU at $d = 2.3$ kpc, the closest of their five astrometric binaries. The apparent V magnitude difference was $\Delta V = 1.0 \pm 0.3$. Sota et al. (2011) find a spectral type of O4.5 V((fc)).

From the standpoint of its X-ray emission, HD 303308 is quite typical of other early-mid type O stars, though we cannot rule out some colliding wind emission in the zone between the two stars. We note that HD 303308 showed some evidence of time variability, with four maximum likelihood blocks, and $P_{\text{KS}} = 20\%$.

6.2.3. Tr16-9 = MJ 481, O9.5 V

Nelan et al. (2010) find a binary separation of 16 ± 2 mas for Tr16-9 = MJ 481, corresponding to ~ 35 AU at $d = 2.3$ kpc, the second closest of their five astrometric binaries. MJ 481 shows low-level time variability, $\log L_X/L_{\text{bol}} = -7.17$, and a higher-than-average $kT_1 = 0.70_{-0.1}^{+0.2}$ keV (Nazé et al. 2011). Like HD 303308, we cannot rule out some colliding wind emission.

6.3. O+O Spectroscopic Binaries

The O+O binaries listed in Table 3 are among the best studied in Carina and among them HD 93403, HD 93205, HD 93343, Tr16-112, and QZ Car have been proposed as colliding wind binaries (Rauw et al. 2009; Morrell et al. 2001; Parkin et al. 2011).

We note however the wide variety of post-shock temperatures in these systems in Table 3. We find that the longer-period O+O spectroscopic binaries like HD 93403 (15.09 d), QZ Car (20.72 d), and HD 93343 (44.15 d) have high kT shocks, and the shorter-period systems like HD 93205 (6.08 d), Tr16-112 (4.02 d), and FO 15 (1.41 d), show only soft X-ray shocks. Figure 13 plots kT_{avg} versus orbital period for the 11 spectroscopic binaries in Table 3. The orbital periods are from the compilations of Rauw et al. (2009); Nelan et al. (2010).

For multiple systems like QZ Car, we use the orbital period of the primary in Fig. 13, because the primary pair accounts for most of the X-ray luminosity. For example, in QZ Car the A1/A2 pair with the O9.7 I primary accounts for $\sim 74\%$ of the system’s X-ray flux (see Table 5, Parkin et al. 2011). For Tr16-110, O7 V + O8 V + O9 V, a 2+1 spectroscopic binary,

the primary and secondary orbital periods are 3.63 and 5.03 days, respectively (Table 7, Rauw et al. 2009). We use $P = 3.63$ in Fig. 13, though both periods are short; either period yields the same correlation. Similarly, for Tr16-104, an eclipsing O7 V + O9.5 V binary bound to a B0.2 IV star, we use the 2.15-d primary orbital period. The orbital period of the B0.2 IV star is either 285 d or 1341 d (Rauw et al. 2001). We ignore the possible contribution of wind shocks with the distant B0.2 IV star.

Fig. 13 shows a correlation between orbital period and kT , with a Pearson’s linear correlation coefficient of 0.95. The correlation hinges on the three long-period systems with $kT_{\text{avg}} > 1$ keV: HD 93403, QZ Car, and HD 93343. A larger sample of O+O binaries is needed to confirm a correlation between orbital period or binary separation and average shock temperature. We note that the wide binaries η Car with $P_{\text{orb}} \approx 5.54$ yr (Gull et al. 2009), and WR 25 (WN6h + O) with $P_{\text{orb}} \approx 207.7$ d (Gamen et al. 2008), are consistent with this correlation.

If such a correlation is confirmed, then the presence of a close, luminous companion (separation $\lesssim 5R_{\star}$) may significantly reduce the observed post-shock temperatures, and thus the wind speed at the shock, whether those shocks are produced throughout the wind (EWS) or in the wind collision zone (CWS). Put another way, there may not be enough room to allow the winds to ramp up to terminal speed. In systems like FO 15 with low L_X/L_{bol} the emission measure and, hence, the density in the X-ray shocks may also be reduced.

Including the astrometric binaries in our analysis, it appears that, as the binary separation increases beyond a few tens of AU, the colliding wind shocks become weaker, as expected from adiabatic expansion (e.g., Antokhin et al. 2004), and the X-rays are dominated by embedded wind shock emission produced within a few R_{\star} . We emphasize that for most O+O binaries, both mechanisms – embedded wind shocks and colliding wind shocks – may be at work.

6.3.1. HD 93403, O5 III(fc) + O7 V

The 15.093-d O5 III(fc) + O7 V eccentric ($e = 0.234$) binary HD 93403 is the most X-ray active O+O binary in Carina, with $\log L_X \approx 33.1$ ergs s $^{-1}$ and $\log L_X/L_{\text{bol}} \approx -6.4$. In the CCCP data, HD 93403 was observed in OBSIDs 9484, 9486 and 9891 (for the observation log see Table 1 of Townsley et al. 2011a). Nazé et al. (2011) fit the combined ACIS-I spectrum with $\log N_{\text{H}}^{\text{ISM}} = 21.49$ cm $^{-2}$, and find $N_{\text{H}}^{\star} = 21.5_{-0.07}^{+0.06}$, $kT_1 = 0.62_{-0.01}^{+0.02}$ and $kT_2 = 1.6_{-0.05}^{+0.06}$, with approximately equal emission measure in each temperature component.

We note that Walborn et al. (2010) recently reclassified the primary of HD 93403 as

O5 III(fc) on the basis of its C III emission lines. Using the common ephemeris of Rauw et al. (2000), $P = 15.093$ d and $T_0 = 51355.14$ MJD, OBSIDs 9486 and 9491 occurred from phase 0.15 to 0.28, and OBSID 9484 occurred from phase 0.44 to 0.48, near apastron, with similar exposure times in each phase range. We note that throughout this study we use the *Chandra* convention $\text{MJD} = \text{HJD} - 2400000.5$, rather than the more common convention $\text{HJD} - 2450000.0$ to express T_0 . The lower left panel of Fig. 9 shows the sequenced light curve of HD 93403.

In the most comprehensive examination of HD 93403’s X-ray light curve to date, Rauw et al. (2002) use a series of *ROSAT* HRI and *XMM-Newton* MOS1 photometry and PN spectra to show a clear orbital modulation of its X-ray luminosity with orbital phase, with X-ray maximum occurring at $\phi = 0.0$ (periastron). The lower mean count rate at the beginning of the HD 93403 light curve, corresponding to $0.44 < \phi < 0.48$, suggests an X-ray minimum near apastron.

The short-term variability seen throughout the three *Chandra* observations, though small, is statistically significant. The rapid variability amplitude varies from 5 – 15%, and is comparable to the 20% long-term variability amplitude reported by Rauw et al. (2002).

Rauw et al. (2002) used a greater distance to Carina, $d = 3.2$ kpc, and a higher ISM column density, $\log N_{\text{H}}^{\text{ISM}} = 21.56 \text{ cm}^{-2}$. They found a 0.5-2.5 keV $\log L_{\text{X}} \approx 33.57 \text{ ergs s}^{-1}$. Applying a distance $d = 2.3$ kpc yields $\log L_{\text{X}} \approx 33.28 \text{ ergs s}^{-1}$ in the 0.5-2.5 keV band for the mean of the four *XMM* observations.

Using Rauw et al. (2002)’s higher ISM column density, we find a CCCP 0.5-2.5 keV $\log L_{\text{X}} \approx 33.19 \text{ ergs s}^{-1}$ during the CCCP observations in 2008 August, only 19% lower than the *XMM-Newton* observations in 2000 December and 2001 February. Overall the CCCP spectral and timing analysis of HD 93403 confirms the results of Rauw et al. (2002).

6.3.2. HD 93205, O3.5 V((f)) + O8 V

Morrell et al. (2001) present the definitive study on HD 93205 from an extensive set of ground-based spectroscopic, *IUE* far ultraviolet, and *ROSAT* X-ray observations. They find a 6.0803 ± 0.0004 -d orbital period, primary and secondary masses of $52 - 60 M_{\odot}$ and $22 - 25 M_{\odot}$, an orbital inclination of about 55° , an orbital eccentricity $e = 0.37$, an apsidal period of 185 ± 16 yr, and phase-locked X-ray variability, with X-ray maximum near periastron.

HD 93205’s CCCP light curve in Fig. 9 shows a slow steady decline over the 1 day observation, which began and ended at MJD 53977.794 and 53978.817. From the combined

ephemeris in Table 4 of Morrell et al. (2001) in which $T_0 = 50498.589$ MJD, OBSID 4495 began at orbital phase $\phi = 0.21 \pm 0.04$ and ended at phase $\phi = 0.38 \pm 0.04$, during which the average X-ray parameters were $\log L_X \approx 32.55$ ergs s $^{-1}$, $\log L_X/L_{\text{bol}} = -6.82$, $kT_1 = 0.23 \pm 0.01$, and $kT_2 = 0.74 \pm 0.03$, with most of the emission measure in the cooler component (Nazé et al. 2011).

This is the end of the declining phase in the *ROSAT* HRI light curve in Fig. 8 of Morrell et al. (2001). Our results thus support the X-ray periodicity of Morrell et al. (2001). Its high L_X/L_{bol} is similar to other binaries with early-O primaries. As with the other short-period binaries, the colliding wind shock temperatures do not exceed 1 keV.

6.3.3. *Tr16-112 = LS 1874 = CPD-59 2641 = MJ 535, O5.5-O6 V(n)((fc)) + B2 V*

Rauw et al. (2009) presented a detailed multiplicity study of three X-ray luminous Carina O stars as part of the X-Mega project³: Tr16-112, HD 93343 and HD 93250. Based on a long series of medium- and high-resolution spectra of Tr16-112, they obtained spectral types of O5.5-6 V((f)) and B2 V, for the primary and secondary. Sota et al. (2011) revised the primary spectral type to O5.5-O6 V(n)((fc)).

Rauw et al. (2009) find an orbital period $P = 4.0157$ d, eccentricity $e = 0.15 \pm 0.01$, inclination $i = 54^{+4}_{-3}$, primary and secondary masses $M_1 = 41.0 \pm 2.5M_{\odot}$ and $M_2 = 11.7 \pm 0.6M_{\odot}$, and periastron passage time $T_0 = 54559.810 \pm 0.060$ MJD. They estimate that the primary fills $\frac{3}{4}$ of its Roche lobe.

In the CCCP data, Tr16-112 was observed in OBSID 6402 in 2006 August during which time it showed no signs of variability, with $P_{\text{KS}} = 53\%$ and only one maximum likelihood block (95% confidence). OBSID 6402 began and ended at MJD 53977.78 and 53978.83, corresponding to orbital phases 0.06 and 0.32 in Tr16-112. That is close to periastron passage, though we note that the orbit is not highly eccentric. This short-period binary has $kT_{\text{avg}} \approx 0.35$ keV.

6.3.4. *HD 93343, O8 V + O7-8.5 V*

Rauw et al. (2009) present the first comprehensive analysis of the double-lined spectroscopic binary HD 93343. They find a set of sharp lines associated with the less massive

³<http://lheawww.gsfc.nasa.gov/users/corcoran/xmega/xmega.html>

O8 V secondary moving in opposite phase to the higher-mass O8 V primary. They note that the spectral type of the secondary could be in the range O7-O8.5 V. They find a period of ≈ 44.15 days, though they were not able to establish an absolute ephemeris.

For HD 93343 we note $\log L_X = 31.66 \pm 0.24$, $\log L_X/L_{\text{bol}} \approx -6.98$, $kT_1 = 0.70_{-0.09}^{+0.13}$, and $kT_2 > 6.5$ keV, with comparable emission measure in each temperature component. HD 93343 showed no evidence of time variability in OBSID 6402.

Antokhin et al. (2008) found $kT_1 = 0.29_{-0.05}^{+0.04}$, $kT_2 = 2.8_{-1.4}^{+1.5}$, and $\log L_X \approx 32.2$, a factor of 3 more luminous in the 0.4-10 keV band with *XMM* than was found in the same band with *Chandra* (Nazé et al. 2011), with most of the added luminosity in the *XMM* fit in the softer component.

Further optical spectroscopic monitoring is needed to establish a firm ephemeris for HD 93343. Further *Chandra* observations would provide a better estimate of the shock temperatures, and a third estimate of L_X to confirm the variability. An X-ray maximum near periastron would signal a colliding-wind binary. Spectropolarimetric monitoring could reveal the presence of large-scale magnetic fields on one or the other star.

For now, we consider HD 93343 a CWS X-ray source, so we include it in Fig. 13. We note though that the hard shocks seen on HD 93343 with *Chandra* are not predicted by Pittard (2009) in their colliding wind binary model CWB3, an O6 V + O8 V binary with a 10.7-d period, the closest model to HD 93343. The predicted temperature distributions are somewhat consistent with the Antokhin et al. (2008) result, however.

6.3.5. The Short-Period Eclipsing Binary FO 15, O5.5 Vz + O9.5 V

The double-lined eclipsing binary FO 15 was first typed by Forte & Orsatti (1981) and studied in detail by Niemela et al. (2006). Its circular period is 1.413560 ± 0.000003 d with $T_0 = 53159.0 \pm 0.2$ MJD, $i \approx 80^\circ$, and primary and secondary masses $M_1 = 30.4 \pm 1.0M_\odot$ and $M_2 = 15.8 \pm 1.0M_\odot$. The stellar radii are $R_1 \approx 7.5R_\odot$ and $R_2 \approx 5.3R_\odot$ and the Roche lobe radii are just $8.3R_\odot$ and $6.15R_\odot$. The semi-major axis is $a = 19.1R_\odot$, implying the photospheres are separated by $\sim 3R_1$.

The “z” spectral type indicates strong He II $\lambda 4686$ absorption suggesting the primary is on the ZAMS (c.f., Walborn & Blades 1997). Located in the south pillars (see Povich et al. 2011b), FO 15 is a ZAMS-age O+O binary, with a separation of only $3R_*$, in a region of active star formation. Moreover, Niemela et al. (2006) note the absence of wind features in both stars at most phases. They suggest that both O dwarfs may be weak-wind stars

(Martins et al. 2005b).

The top left panel of Fig. 9 shows the sequenced light curve of FO 15, showing a steady decline from the beginning of the first observation through the end of the second. OBSID 6402 began and ended at MJD 53977.78 and 53978.83, corresponding to orbital phases $\phi = 0.231 \pm 0.001$ and 0.978 ± 0.001 . OBSID 9483 began and ended at MJD 54706.97 and 54707.68, corresponding to orbital phases $\phi = 0.083 \pm 0.002$ and 0.591 ± 0.002 . Note that OBSIDs 6402 and 9483 were separated by nearly 729 days, i.e., 515 orbital cycles.

FO 15 is noteworthy because it has the lowest L_X/L_{bol} of any O binary in the CCCP: $\log L_X/L_{\text{bol}} = -7.65$. It is relatively soft with $kT = 0.5 \pm 0.3$ keV, yet it is clearly time variable. It is very young, it has the shortest orbital period in our sample, and it is one of only four weak-wind systems in Carina (see also Nazé et al. 2011).

The soft X-ray spectrum of FO 15 (indicating low-velocity shocks) and low L_X/L_{bol} (indicating low shock densities) suggest that in very close, short-period binaries the winds may not have reached v_∞ when they collide, or alternatively, the luminous companion may inhibit wind acceleration and mass-loss via radiative braking (Gayley et al. 1997) as a result of non-radial radiative forces (from the distorted shape of the star).

6.4. B Stars

B stars provide a transition in the X-ray properties of massive stars. Early B stars are often detected in X-rays, though their detection fraction is typically less than 50%. Like most late-O stars, B stars are often soft, low L_X/L_{bol} sources (Cohen et al. 1997; Evans et al. 2003), but in some cases they are particularly hard and strong X-ray sources (e.g. τ Sco, B0.2 V), which has a complex magnetic geometry (Donati et al. 2006b). The Carina Nebula Complex objects provide an excellent sample to explore this interesting spectral region further.

Evans et al. (2011) examine a group of photometrically selected, candidate late-B stars in Tr 16. For this group, Evans et al. (2011) find no stars with $\log L_X > 31$ and suggest that the X-ray detected late-B stars in Tr 16 probably harbor unseen, lower-mass, late-type pre-main sequence companions.

With regard to the B stars, the main results of this study are that (i) many B stars with moderate X-ray fluxes ($\log f_X < -14$ ergs cm⁻² s⁻¹, corresponding approximately to $\log L_X < 31$ ergs s⁻¹) probably harbor unseen, coronal PMS companions, and (ii) that most of the B stars with very high X-ray fluxes ($\log f_X > -14$ ergs cm⁻² s⁻¹, corresponding approximately to $\log L_X > 31$ ergs s⁻¹), *cannot* be accounted for by unseen, coronal companions.

Because their winds are too weak to produce much embedded wind shock emission, these active B stars may be similar to the magnetic B stars like τ Scorpii, B0.2 V (Cohen et al. 2003; Donati et al. 2006b; Petit et al. 2011) or the He-strong B2 Vp stars like σ Ori E (Shore & Brown 1990; Sanz-Forcada et al. 2004; Townsend & Owocki 2005).

Thus, the X-ray active B stars at the top of Table 4 merit detailed follow-up ground-based spectroscopic, photometric, and spectro-polarimetric monitoring. Below we discuss the two most remarkable B stars in the CCCP survey in more detail.

6.4.1. *The Candidate Herbig Be Star SS73 24*

The most X-ray active B star in Carina is the emission-line star Hen 3-485 = Tr 16 MJ 640 = SS73 24 = WRA 642, with $\log L_X = 31.70$ and $\log L_X/L_{\text{bol}} = -5.65$. SS73 24 was classified by Sanduleak and Stephenson (1973) as Be! pec, remarking in the footnote to their Table 1, “Our plates show numerous weak emission lines some of which appear to be Fe II or [Fe II].” SS73 24 is located close to the Treasure Chest Cluster (Smith et al. 2005) in the southern portion of the Carina Nebula, and is a strong infrared emission source (see Fig. 14).

Based on its emission lines, spectral type, and strong infrared excess, Miroshnichenko (2007) classified Hen 3-485 = SS73 24 as a dust-forming B[e] star, and listed it as a candidate FS CMa star. He proposed, “that these objects are binary systems that are currently undergoing or have recently undergone a phase of rapid mass exchange, associated with a strong mass loss and dust formation. A new name, FS CMa stars, and classification criteria are proposed for the unclassified B[e] stars.” Based on its X-ray and infrared emission, and its association with the star-forming Treasure Chest cluster, we show that SS73 24 is most likely a young, accreting Herbig Be star, not an evolved B[e] binary.

In Fig. 14a we show the UBV/JHK/IRAC/MIPS 0.3 – 24 μm SED of SS73 24, though we note that the Spitzer-Vela Survey IRAC 3.5 – 8 μm photometry is mildly saturated. Moreover, its $U - B = -0.71$ and $B - V = 0.70$ colors indicate relatively strong emission-line veiling, which we do not model.

The UBV/JHK/MIPS photometry were fit using the Robitaille et al. (2006) YSO models. The SED fitting method described by Povich et al. (2011b) generates a set of best-fit models from a large grid of star/disk/envelope models. The set of most likely models yields the following parameters: $L_{\text{bol}} = 6\,000 \pm 2\,000 L_{\odot}$, $T_{\text{eff}} = 25\,000 \pm 1\,400$ K, and $A_V = 2.0 \pm 0.2$ mag, consistent with a 9-11 M_{\odot} B2 dwarf, a warm accretion disk, and a cooler circumstellar envelope (blue, green, and red curves, respectively, in Fig. 14b).

SS73 24 was observed for 69 ks during OBSID 6578 and 9483, separated by ~ 400 days. It showed no strong short-term variability during either observation, and no long-term variability between observations. Its grouped ACIS spectrum was fit with a single-temperature, solar-abundance APEC emission model, and two TBABS absorption components: one fixed at $N_{\text{H}} = 3.2 \times 10^{21} \text{ cm}^{-2}$ representing ISM absorption with $A_V = 2.0$ mag, the other column density (a free parameter) to represent circumstellar absorption from the disk/envelope. We note that SS73 24 is the most X-ray luminous B star in Carina with $\log L_X \approx 31.7 \text{ ergs s}^{-1}$, and one of the hardest with $kT \sim 3 \text{ keV}$, comparable to only a few other known Herbig Be stars (Hamaguchi et al. 2000; Zinnecker & Preibisch 1994; Stelzer et al. 2006).

It should be noted that the origin of hard X-rays on Herbig Be stars is not known. Vink et al. (2005) show that the flaring X-ray Herbig Be star MCW 297 has an astrometric binary companion (a lower-mass PMS star) that may be the source of the hard X-ray flare. That said, SS73 24 is not flaring in the CCCP data and its L_X is higher than any other non-flaring PMS star in the CCCP.

6.4.2. HD 93501, B1.5 III:

The B1.5 III: star HD 93501=Coll 228 96 was detected by Levato et al. (1990) as SB2, though no orbital parameters were published. The star is noteworthy because of its extremely hard X-ray spectrum, that we model as very hot thermal plasma ($kT > 6 \text{ keV}$, 90% confidence lower bound), with little excess column density. Its spectrum can also be fit a power-law with index $\Gamma = 1.3 \pm 0.2$. Assuming HD 93501 is a member of the Collinder 228 cluster at $d = 2.3 \text{ kpc}$, its $\log L_X \approx 31.1 \text{ ergs s}^{-1}$. It was observed in three *Chandra* OBSIDs with no indication of long- or short-term variability. HD 93501’s very hard spectrum, high L_X , and lack of variability is not typical of coronal PMS stars. HD 93501’s X-ray spectrum is unique among the 78 OB stars with more than 50 counts.

7. Summary and Discussion

We have assembled an optical/X-ray catalog of the 200 known O and early-B stars in the *Chandra* Carina Complex Project to study the X-ray emission mechanisms on young, massive stars. Like Nazé et al. (2011), we find that most O stars in Carina approximately follow the well-established relation between L_X and L_{bol} , and generally have soft X-ray spectra, with characteristic temperatures $kT < 0.8 \text{ keV}$.

There are numerous examples of O and B stars, though, that do not follow this trend.

We examine their X-ray properties with an eye to classifying their primary underlying X-ray emission mechanism as (1) embedded wind shocks, (2) colliding wind shocks, (3) magnetically confined wind shocks, (4) low-mass, coronal PMS companions, or (5) some other mechanism, possibly related to magnetic fields.

Fig. 4 provides a good overview of the X-ray/optical data: $\approx \frac{2}{3}$ of the O and early-B stars lie on the cool side of the L_X/L_{bol} versus kT diagram. Most of these stars have X-ray properties consistent with embedded wind shock sources, with a characteristic average $kT \approx 0.5$ keV and $\log L_X/L_{\text{bol}} \approx -7.2$.

Some of the well-known spectroscopic binaries in Table 3 also lie on the cool side of Fig. 4a, suggesting perhaps a universal X-ray emission mechanism for all O stars. However, Fig. 13 suggests a different trend. It shows a correlation between orbital period and kT , with a Pearson’s linear correlation coefficient of 0.95. The correlation, which hinges on the longest-period binaries, requires confirmation using a larger sample of binaries.

If the trend is confirmed, we suggest that in short-period binaries like HD 93205 and FO 15, the winds have not reached v_∞ when they collide or, alternatively, the luminous companion may inhibit wind acceleration via radiative braking or some other mechanism (Gayley et al. 1997). In some very wide systems like HD 93129A, O2 If*, it appears that embedded wind shocks (close to the O2 photosphere of Aa) and colliding wind shocks in the far wind collision zone between Aa and Ab are both at work.

Then there is the curious case of HD 93250, the O4 III(fc) star. We argue in §6.2.1 (see also Rauw et al. 2009) that HD 93250’s strong X-ray and radio emission are evidence for colliding wind shocks. Given the kT versus P_{orb} trend seen in Fig. 13, we suggest that it could be an O+O binary with a period > 30 days, and/or a magnetic O star, and that further observations are needed: multi-frequency radio interferometry to measure its spectral index, ground-based optical interferometry to look for a luminous companion, and optical spectro-polarimetry to look for surface magnetic fields.

We are left with two additional candidate magnetic O stars with high L_X/L_{bol} and kT : Tr16-22 = MJ 496, O8.5 V, and CPD-59 2610 = MJ 449 = LS 1865, O8.5 V((f)). So far, magnetic fields have not been reported on any Carina OB stars.

Among the B stars, Fig. 8, shows a large population of B stars, some X-ray detected, some not, whose photon fluxes and upper limits are consistent with a distribution of unseen, low-mass, coronal PMS stars. Superposed on this distribution is a group of B stars whose high- L_X cannot be explained by a distribution of ordinary coronal, PMS companions. The situation here is reminiscent of the X-ray active Herbig Be stars: either their companions are hyperactive compared to other low-mass PMS stars, or there is some intrinsic magnetic

mechanism in these B stars. The dozen or so B stars near the top of Table 4 could, for example, be related to the magnetic B stars like τ Sco, or the He-strong Bp stars.

The B star with the highest L_X and the OB star with the highest L_X/L_{bol} , SS73 24, is located adjacent to the pillar in the Treasure Chest Cluster (see Fig. 15), and it shows a prominent mid-infrared excess (Fig. 14). We model its $0.3 - 24 \mu\text{m}$ SED as an accretion disk + envelope + B2 photosphere. SS73 24 appears to be the first Herbig Be star in Carina.

This research has made extensive use of the SIMBAD and *Vizier* databases, operated at CDS, Strasbourg, France. This work was partially supported by SAO/*Chandra* X-ray Observatory grants GO8-9014X and G09-0019A (PI: Gagné). The CCCP is supported by *Chandra* X-ray Observatory grant GO8-9131X (PI: Townsley) and by the ACIS Instrument Team contract SV4-74018 (PI: Garmire), issued by the *Chandra* X-ray Center, which is operated by the Smithsonian Astrophysical Observatory for and on behalf of NASA under contract NAS8-03060. AFJM is grateful to NSERC (Canada) and FQRNT (Québec) for financial assistance. NRW acknowledges the support of the Space Telescope Science Institute, operated by the Association of Universities for Research in Astronomy, Inc., under NASA contract NAS5-26555. MSP is supported by an NSF Astronomy and Astrophysics Postdoctoral Fellowship under award AST-0901646. The authors wish to thank the anonymous referee for many helpful suggestions.

Facilities: CXO (ACIS).

A. Appendix: *Chandra* Spectral Analysis of HD 93250

In addition to the CCCP ACIS-I observation of Tr14 (OBSID 4495), HD 93250 was observed far off-axis in seven additional grating observations of η Car. Even though HD 93250 is located $\sim 7.5'$ NNW of η Car, the satellite roll angle placed HD 93250 on one of the ACIS-S chips during many of the η Car monitoring observations. Even though the PSF is quite large at $7.5'$ off-axis, HD 93250 is the only bright source there. Pileup was mitigated by the effects of comatic aberration and vignetting at those off-axis angles, and the reduced effective area in zeroth order. The *Chandra* observation log is shown in Table 5.

The data were reduced in the usual way (see Broos et al. 2011a) and spectra were extracted using the *CIAO* tool `psextract` using a $12''$ source circle, and a nearby source-free background region, away from the dispersed HEG and MEG spectra of η Car. The spectra were grouped using the *ACIS Extract* tool `ae_group_spectra`. The ACIS-S spectra were merged with the *CIAO* tool `acisspec` for a combined exposure time of 238 ks (see Table 5).

We note that Evans et al. (2004) performed a similar wind-absorption analysis of the OBSID 6402 ACIS-I spectrum of HD 93250, and found two temperature components at 0.55 and 2.33 keV.

To exploit the high S/N of the merged ACIS-S spectrum, we fit a rather complex XSPEC spectral model. As before, we modeled the cold, neutral ISM with TBABS, freezing $\log N_{\text{H}}^{\text{ISM}} = 21.48$. Assuming that some of the emission arises from embedded wind shocks close to HD 93250, and that the harder emission forms in colliding wind shocks where the wind is less dense, we used a WINDTABS absorption component (Leutenegger et al. 2010) for the cool emission component. The main advantage of WINDTABS over TBABS is that (i) it is not a simple slab model – the emission and absorption is distributed radially throughout the wind via a specified onset shock radius and wind velocity law, and (ii) the absorption model accounts for the ionization of the wind. The only free parameter in WINDTABS is the characteristic mass column in g cm^{-2} ,

$$\Sigma_{\star} = \frac{\dot{M}}{4\pi R_{\star} v_{\infty}}.$$

To estimate the distribution of absorbing material in the wind of HD 93250 we adopt wind parameters $R_0 = 1.5R_{\star}$ (the onset radius for X-ray shocks) and $\beta = 0.7$ (the wind velocity law) that are consistent with recent X-ray line-profile measurements of O supergiants (Cohen et al. 2010, 2006). We note that a direct finite-disk corrected CAK (Castor et al. 1975) model with fixed \bar{Q} and α also produces $\beta \approx 0.75$.

For the APEC emission model and the WINDTABS and TBABS absorption models we adopt the solar abundance values of Asplund et al. (2009). Though we expect differing levels of CNO processed material in the atmospheres and winds of the Carina O stars, we note that the CNO lines and absorption edges occur longward of 20 Å where the *Chandra* ACIS-I spectra are extremely weak. The ACIS spectra are truncated below 0.5 keV (above 25 Å).

The best-fit TBABS(WINDTABS(APEC)+APEC+APEC) model is shown in Fig. 11 in red. The ACIS-I and ACIS-S spectra were then fit individually to measure L_{X} during each OBSID. In Fig. 12, we merged the last three spectra, OBSID 7341, 7342 and 7189 from 2006 June.

The best-fit mass column $\Sigma_{\star} = 0.03 \pm 0.01 \text{ g cm}^{-2}$ yields a time-averaged ISM-corrected X-ray luminosity $\log L_{\text{X}} = 33.18$. We note that this is very close to the value found by Nazé et al. (2011) fitting only the ACIS-I data without WINDTABS, $\log L_{\text{X}} = 33.19$. The benefit of using WINDTABS is that it provides a physically meaningful estimate of the wind mass column.

Using a terminal wind speed $v_{\infty} = 3000 \text{ km s}^{-1}$ (Martins et al. 2005b) and a radius

$R = 17.7R_{\odot}$ implied by $\log L_{\text{bol}}/L_{\odot} = 5.95$ and $\log T_{\text{eff}} = 4.62$, the best-fit mass column yields a mass-loss rate $\dot{M} = 1.4 \pm 0.5 \times 10^{-6} M_{\odot} \text{ yr}^{-1}$.

REFERENCES

- Albacete Colombo, J. F., Morrell, N. I., Rauw, G., Corcoran, M. F., Niemela, V. S., & Sana, H. 2002, *MNRAS*, 336, 1099
- Albacete-Colombo, J. F., Damiani, F., Micela, G., Sciortino, S., & Harnden, F. R., Jr. 2008, *A&A*, 490, 1055
- Antokhin, I. I., Owocki, S. P., & Brown, J. C. 2004, *ApJ*, 611, 434
- Antokhin, I. I., Rauw, G., Vreux, J.-M., van der Hucht, K. A., & Brown, J. C. 2008, *A&A*, 477, 593
- Babel, J., & Montmerle, T. 1997, *ApJ*, 485, L29
- Benaglia, P., Koribalski, B., & Albacete Colombo, J. F. 2006, *PASA*, 23, 50
- Benaglia, P., Dougherty, S. M., Phillips, C., Koribalski, B., & Tzioumis, T. 2010, *Revista Mexicana de Astronomia y Astrofisica Conference Series*, 38, 41
- Berghoefter, T. W., Schmitt, J. H. M. M., Danner, R., & Cassinelli, J. P. 1997, *A&A*, 322, 167
- Bessell, M. S., Castelli, F., & Plez, B. 1998, *A&A*, 333, 231
- Briggs, K. R., & Pye, J. P. 2003, *MNRAS*, 345, 714
- Broos, P. S., Townsley, L. K., Feigelson, E. D., Getman, K. V., Bauer, F. E., & Garmire, G. P. 2010, *ApJ*, 714, 1582
- Broos, P. S., et al. 2011, *ApJS*, submitted (CCCP Catalog Paper)
- Caillault, J.-P., Gagné, M., & Stauffer, J. R. 1994, *ApJ*, 432, 386
- Cassinelli, J. P., Miller, N. A., Waldron, W. L., MacFarlane, J. J., & Cohen, D. H. 2001, *ApJ*, 554, L55
- Cassinelli, J. P., Ignace, R., Waldron, W. L., Cho, J., Murphy, N. A., & Lazarian, A. 2008, *ApJ*, 683, 1052

- Castelli, F., & Kurucz, R. L. 2004, arXiv:astro-ph/0405087
- Castor, J. I., Abbott, D. C., & Klein, R. I. 1975, ApJ, 195, 157
- Cohen, D. H., Cassinelli, J. P., & Macfarlane, J. J. 1997, ApJ, 487, 867
- Cohen, D. H., de Messières, G. E., MacFarlane, J. J., Miller, N. A., Cassinelli, J. P., Owocki, S. P., & Liedahl, D. A. 2003, ApJ, 586, 495
- Cohen, D. H., Leutenegger, M. A., Grizzard, K. T., Reed, C. L., Kramer, R. H., & Owocki, S. P. 2006, MNRAS, 368, 1905
- Cohen, D. H., Leutenegger, M. A., Wollman, E. E., Zsargó, J., Hillier, D. J., Townsend, R. H. D., & Owocki, S. P. 2010, MNRAS, 405, 2391
- Cohen, D. H., Wollman, E. E., & Leutenegger, M. A. 2011, arXiv:1009.5669, Proceedings of IAU Symposium 272: Active OB Stars
- Corcoran, M. F., et al. 2001, ApJ, 562, 1031
- Daniel, K. J., Linsky, J. L., & Gagné, M. 2002, ApJ, 578, 486
- Davidson, K., & Ostriker, J. P. 1973, ApJ, 179, 585
- De Becker, M., Rauw, G., Pittard, J. M., Antokhin, I. I., Stevens, I. R., Gosset, E., & Owocki, S. P. 2004, A&A, 416, 221
- De Becker, M. 2007, A&A Rev., 14, 171
- DeGioia-Eastwood, K., Throop, H., Walker, G., & Cudworth, K. M. 2001, ApJ, 549, 578
- de Jager, C., & Nieuwenhuijzen, H. 1987, A&A, 177, 217
- Dessart, L., & Owocki, S. P. 2005, A&A, 437, 657
- Dessart, L., & Owocki, S. P. 2005, A&A, 432, 281
- Donati, J.-F., Babel, J., Harries, T. J., Howarth, I. D., Petit, P., & Semel, M. 2002, MNRAS, 333, 55
- Donati, J.-F., Howarth, I. D., Bouret, J.-C., Petit, P., Catala, C., & Landstreet, J. 2006, MNRAS, 365, L6
- Donati, J.-F., et al. 2006, MNRAS, 370, 629

- Donati, J.-F., & Landstreet, J. D. 2009, *ARA&A*, 47, 333
- Dougherty, S. M., & Williams, P. M. 2000, *MNRAS*, 319, 1005
- Drake, S. A., Linsky, J. L., Schmitt, J. H. M. M., & Rosso, C. 1994, *ApJ*, 420, 387
- Evans, N. R., Seward, F. D., Krauss, M. I., Isobe, T., Nichols, J., Schlegel, E. M., & Wolk, S. J. 2003, *ApJ*, 589, 509
- Evans, N. R., Schlegel, E. M., Waldron, W. L., Seward, F. D., Krauss, M. I., Nichols, J., & Wolk, S. J. 2004, *ApJ*, 612, 1065
- Evans, N. R., et al. 2011, *ApJS*, submitted (CCCP Tr16 B Stars Paper)
- Feigelson, E. D., Broos, P., Gaffney, J. A., III, Garmire, G., Hillenbrand, L. A., Pravdo, S. H., Townsley, L., & Tsuboi, Y. 2002, *ApJ*, 574, 258
- Feigelson, E. D., et al. 2011, *ApJS*, submitted (CCCP Clustering Paper)
- Feldmeier, A., Puls, J., & Pauldrach, A. W. A. 1997, *A&A*, 322, 878
- Feldmeier, A., Oskinova, L., & Hamann, W.-R. 2003, *A&A*, 403, 217
- Forte, J. C. 1976, *A&AS*, 25, 271
- Forte, J. C., & Orsatti, A. M. 1981, *AJ*, 86, 209
- Freyhammer, L., Clausen, J., Arentoft, T., & Sterken, C. 2001, *Eta Carinae and Other Mysterious Stars: The Hidden Opportunities of Emission Spectroscopy*, 242, 195
- Gagné, M., Caillault, J.-P., & Stauffer, J. R. 1995, *ApJ*, 450, 217
- Gagne, M., Caillault, J.-P., Stauffer, J. R., & Linsky, J. L. 1997, *ApJ*, 478, L87
- Gagné, M., Oksala, M. E., Cohen, D. H., Tonnesen, S. K., ud-Doula, A., Owocki, S. P., Townsend, R. H. D., & MacFarlane, J. J. 2005, *ApJ*, 628, 986
- Gamen, R., et al. 2008, *Revista Mexicana de Astronomia y Astrofisica Conference Series*, 33, 91
- Gayley, K. G., Owocki, S. P., & Cranmer, S. R. 1997, *ApJ*, 475, 786
- Getman, K. V., Feigelson, E. D., Grosso, N., McCaughrean, M. J., Micela, G., Broos, P., Garmire, G., & Townsley, L. 2005, *ApJS*, 160, 353

- Gosset, E., Nazé, Y., Sana, H., Rauw, G., & Vreux, J.-M. 2009, *A&A*, 508, 805
- Gull, T. R., et al. 2009, *MNRAS*, 396, 1308
- Hamaguchi, K., Terada, H., Bamba, A., & Koyama, K. 2000, *ApJ*, 532, 1111
- Herbst, W. 1976, *ApJ*, 208, 923
- Hillier, D. J., & Lanz, T. 2001, *Spectroscopic Challenges of Photoionized Plasmas*, 247, 343
- Hoffmeister, V. H., Chini, R., Scheyda, C. M., Schulze, D., Watermann, R., Nürnberger, D., & Vogt, N. 2008, *ApJ*, 686, 310
- Ignace, R., Oskinova, L. M., Jardine, M., Cassinelli, J. P., Cohen, D. H., Donati, J.-F., Townsend, R. H. D., & ud-Doula, A. 2010, *ApJ*, 721, 1412
- Kahn, S. M., Leutenegger, M. A., Cottam, J., Rauw, G., Vreux, J.-M., den Boggende, A. J. F., Mewe, R., Güdel, M. 2001, *A&A*, 365, L312
- Kroupa, P. 2002, *Science*, 295, 82
- Leitherer, C., Chapman, J. M., & Koribalski, B. 1995, *ApJ*, 450, 289
- Lépine, S., & Moffat, A. F. J. 1999, *ApJ*, 514, 909
- Lépine, S., et al. 2000, *AJ*, 120, 3201
- Leutenegger, M. A., Cohen, D. H., Zsargó, J., Martell, E. M., MacArthur, J. P., Owocki, S. P., Gagné, M., & Hillier, D. J. 2010, *ApJ*, 719, 1767
- Levato, H., Malaroda, S., Garcia, B., Morrell, N., & Solivella, G. 1990, *ApJS*, 72, 323
- Lucy, L. B., & White, R. L. 1980, *ApJ*, 241, 300
- Lucy, L. B. 1982, *ApJ*, 255, 286
- Marchenko, S. V., Moffat, A. F. J., St-Louis, N., & Fullerton, A. W. 2006, *ApJ*, 639, L75
- Maíz Apellániz, J., et al. 2010, *arXiv:1010.5680*
- Maiz Apellaniz, J. 2007, *HST Proposal*, 11294
- Martins, F., Schaerer, D., & Hillier, D. J. 2005, *A&A*, 436, 1049
- Martins, F., Schaerer, D., Hillier, D. J., Meynadier, F., Heydari-Malayeri, M., & Walborn, N. R. 2005, *A&A*, 441, 735

- Martins, F., & Plez, B. 2006, A&A, 457, 637
- Massey, P., & Johnson, J. 1993, AJ, 105, 980
- Massey, P., DeGioia-Eastwood, K., & Waterhouse, E. 2001, AJ, 121, 1050
- Mermilliod, J.-C. 1994, Bulletin d'Information du Centre de Donnees Stellaires, 45, 3
- Moffat, A. F. J. 2008, Clumping in Hot-Star Winds, 17
- Morgan, W. W., Code, A. D., & Whitford, A. E. 1955, ApJS, 2, 41
- Morrell, N., Garcia, B., & Levato, H. 1988, PASP, 100, 1431
- Morrell, N. I., et al. 2001, MNRAS, 326, 85
- Morrison, N. D., & Conti, P. S. 1980, ApJ, 239, 212
- Mullan, D. J., & MacDonald, J. 2005, MNRAS, 356, 1139
- Mullan, D. J., & Waldron, W. L. 2006, ApJ, 637, 506
- Nazé, Y., Rauw, G., Pollock, A. M. T., Walborn, N. R., & Howarth, I. D. 2007, MNRAS, 375, 145
- Nazé, Y. 2009, A&A, 506, 1055
- Nazé, Y., Ud-Doula, A., Spano, M., Rauw, G., De Becker, M., & Walborn, N. R. 2010, A&A, 520, A59
- Nazé, Y., et al. 2011, ApJS, submitted (CCCP Massive Star L_X/L_{bol} Paper)
- Nelan, E. P., Walborn, N. R., Wallace, D. J., Moffat, A. F. J., Makidon, R. B., Gies, D. R., & Panagia, N. 2004, AJ, 128, 323
- Nelan, E. P., Walborn, N. R., Wallace, D. J., Moffat, A. F. J., Makidon, R. B., Gies, D. R., & Panagia, N. 2010, AJ, 139, 2714
- Niemela, V. S., Morrell, N. I., Fernández Lajús, E., Barbá, R., Albacete Colombo, J. F., & Orellana, M. 2006, MNRAS, 367, 1450
- Oskinova, L. M., Hamann, W.-R., Feldmeier, A. 2007, A&A, 476, 1331
- Owocki, S. P., Castor, J. I., & Rybicki, G. B. 1988, ApJ, 335, 914
- Owocki, S. P., & Cohen, D. H. 1999, ApJ, 520, 833

- Pallavicini, R., Golub, L., Rosner, R., Vaiana, G. S., Ayres, T., & Linsky, J. L. 1981, *ApJ*, 248, 279
- Parkin, E. R., et al. 2011, *ApJS*, submitted (CCCP QZ Car Paper)
- Patience, J., Zavala, R. T., Prato, L., Franz, O., Wasserman, L., Tycner, C., Hutter, D. J., & Hummel, C. A. 2008, *ApJ*, 674, L97
- Pereira, C. B., Franco, C. S., & de Araújo, F. X. 2003, *A&A*, 397, 927
- Petit, V., Wade, G. A., Drissen, L., Montmerle, T., & Alecian, E. 2008, *MNRAS*, 387, L23
- Petit, V., Massa, D. L., Marcolinot, W. L. F., Wade, G. A., & Ignace, R. 2011, *MNRAS*, in press
- Pittard, J. M. 2009, *MNRAS*, 396, 1743
- Pollock, A. M. T., Corcoran, M. F., Stevens, I. R., & Williams, P. M. 2005, *ApJ*, 629, 482
- Pollock, A. M. T. 2007, *A&A*, 463, 1111
- Povich, M. S., et al. 2011, *ApJS*, submitted (CCCP Massive Star Candidates Paper)
- Povich, M. S., et al. 2011, *ApJS*, submitted (CCCP IR YSOs Paper)
- Preibisch, T., et al. 2011, *ApJS*, submitted (CCCP HAWK-I Paper)
- Puls, J., et al. 1996, *A&A*, 305, 171
- Raassen, A. J. J., van der Hucht, K. A., Miller, N. A., & Cassinelli, J. P. 2008, *A&A*, 478, 513
- Rauw, G., Sana, H., Gosset, E., Vreux, J.-M., Jehin, E., & Parmentier, G. 2000, *A&A*, 360, 1003
- Rauw, G., Nazé, Y., Carrier, F., Burki, G., Gosset, E., & Vreux, J.-M. 2001, *A&A*, 368, 212
- Rauw, G., Vreux, J.-M., Stevens, I. R., Gosset, E., Sana, H., Jamar, C., & Mason, K. O. 2002, *A&A*, 388, 552
- Rauw, G., Nazé, Y., Fernández Lajús, E., Lanotte, A. A., Solivella, G. R., Sana, H., & Gosset, E. 2009, *MNRAS*, 398, 1582
- Reed, C. 2005, *VizieR Online Data Catalog*, 5125, 0

- Robitaille, T. P., Whitney, B. A., Indebetouw, R., Wood, K., & Denzmore, P. 2006, *ApJS*, 167, 256
- Robitaille, T. P., Whitney, B. A., Indebetouw, R., & Wood, K. 2007, *ApJS*, 169, 328
- Sana, H., Rauw, G., Nazé, Y., Gosset, E., & Vreux, J.-M. 2006, *MNRAS*, 372, 661
- Sana, H., Gosset, E., Rauw, G., Sung, H., & Vreux, J.-M. 2006, *A&A*, 454, 1047
- Sanchawala, K., Chen, W.-P., Lee, H.-T., Chu, Y.-H., Nakajima, Y., Tamura, M., Baba, D., & Sato, S. 2007, *ApJ*, 656, 462
- Sanz-Forcada, J., Franciosini, E., & Pallavicini, R. 2004, *A&A*, 421, 715
- Schulz, N. S., Testa, P., Huenemoerder, D. P., Ishibashi, K., & Canizares, C. R. 2006, *ApJ*, 653, 636
- Shore, S. N., & Brown, D. N. 1990, *ApJ*, 365, 665
- Smith, N. 2006, *ApJ*, 644, 1151
- Skiff, B. A. 2009, *VizieR Online Data Catalog*, 1, 2023
- Skinner, S. L., Güdel, M., Audard, M., & Smith, K. 2004, *ApJ*, 614, 221
- Skinner, S. L., Sokal, K. R., Cohen, D. H., Gagné, M., Owocki, S. P., & Townsend, R. D. 2008, *ApJ*, 683, 796
- Skinner, S. L., Zhekov, S. A., Güdel, M., Schmutz, W., & Sokal, K. R. 2010, *AJ*, 139, 825
- Smith, N., Stassun, K. G., & Bally, J. 2005, *AJ*, 129, 888
- Smith, N. 2006, *MNRAS*, 367, 763
- Spruit, H. C. 2002, *A&A*, 381, 923
- Sota, A., Maíz Apellániz, J., Walborn, N.R., Alfaro, E.J., Barbá, R.H., Morrell, N.I., Gamen, R.C., & Arias, J.I. 2011, *ApJS*, submitted
- Stelzer, B., Flaccomio, E., Montmerle, T., Micela, G., Sciortino, S., Favata, F., Preibisch, T., & Feigelson, E. D. 2005, *ApJS*, 160, 557
- Stelzer, B., Micela, G., Hamaguchi, K., & Schmitt, J. H. M. M. 2006, *A&A*, 457, 223
- Stevens, I. R., Blondin, J. M., & Pollock, A. M. T. 1992, *ApJ*, 386, 265

- Tapia, M., Roth, M., Vázquez, R. A., & Feinstein, A. 2003, *MNRAS*, 339, 44
- Townsend, R. H. D., & Owocki, S. P. 2005, *MNRAS*, 357, 251
- Townsend, R. H. D., Owocki, S. P., & Ud-Doula, A. 2007, *MNRAS*, 382, 139
- Townsend, R. H. D. 2008, *MNRAS*, 389, 559
- Townsley, L. K., et al. 2011, *ApJS*, submitted (CCCP Intro Paper)
- Turner, D. G., Grieve, G. R., Herbst, W., & Harris, W. E. 1980, *AJ*, 85, 1193
- Turner, D. G., & Moffat, A. F. J. 1980, *MNRAS*, 192, 283
- ud-Doula, A., & Owocki, S. P. 2002, *ApJ*, 576, 413
- Vazquez, R. A., Baume, G., Feinstein, A., & Pado, P. 1996, *Revista Mexicana de Astronomia y Astrofisica Conference Series*, 4, 131
- Vink, J. S., O’Neill, P. M., Els, S. G., & Drew, J. E. 2005, *A&A*, 438, L21
- Vuong, M. H., Montmerle, T., Grosso, N., Feigelson, E. D., Verstraete, L., & Ozawa, H. 2003, *A&A*, 408, 581
- Wade, G. A., Fullerton, A. W., Donati, J.-F., Landstreet, J. D., Petit, P., & Strasser, S. 2006, *A&A*, 451, 195
- Walborn, N. R. 1995, *Revista Mexicana de Astronomia y Astrofisica Conference Series*, 2, 51
- Walborn, N. R., & Blades, J. C. 1997, *ApJS*, 112, 457
- Walborn, N. R., et al. 2002, *AJ*, 123, 2754
- Walborn, N. R., Nichols, J. S., & Waldron, W. L. 2009, *ApJ*, 703, 633
- Walborn, N. R., Sota, A., Maíz Apellániz, J., Alfaro, E. J., Morrell, N. I., Barbá, R. H., Arias, J. I., & Gamen, R. C. 2010, *ApJ*, 711, L143
- Waldron, W. L., & Cassinelli, J. P. 2009, *ApJ*, 692, L76
- Wegner, W. 1994, *MNRAS*, 270, 229
- Wojdowski, P. S., & Schulz, N. S. 2005, *ApJ*, 627, 953

Wolk, S. J., Harnden, F. R., Jr., Flaccomio, E., Micela, G., Favata, F., Shang, H., & Feigelson, E. D. 2005, *ApJS*, 160, 423

Wright, N. J., Drake, J. J., Drew, J. E., & Vink, J. S. 2010, *ApJ*, 713, 871

Zhekov, S. A., & Palla, F. 2007, *MNRAS*, 382, 1124

Zinnecker, H., & Preibisch, T. 1994, *A&A*, 292, 152

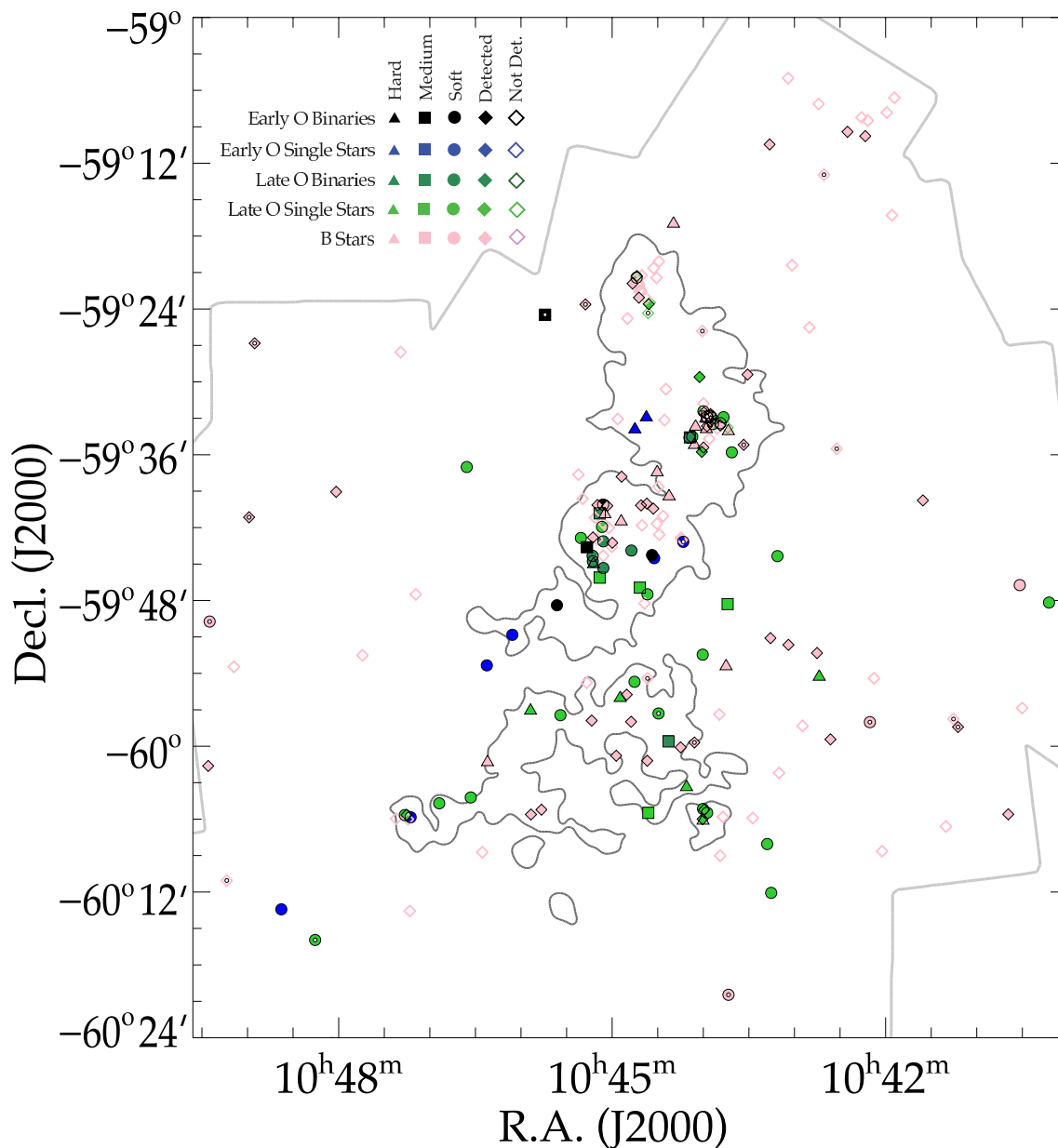


Fig. 1.— Spatial distribution of the 200 OB stars with determined spectral types in Carina. Stars detected in the CCCP are shown as filled symbols. Early-O binaries are black, early-O single stars are blue, late-O binaries are dark green, late-O single stars are light green, and B stars are pink. For the 78 OB stars with more than 50 counts hard, medium, and soft X-ray stars are shown as triangles, squares, and circles, respectively. The 51 X-ray detected stars with fewer than 50 counts are shown as filled diamonds. The open diamonds represent undetected stars (mostly B stars, in pink). The grey outline shows the boundaries of the CCCP and the contours show boundaries of the large-scale clustering of low-mass stars, reproduced from Figure 1 of Feigelson et al. (2011). See §4 for symbol definitions.

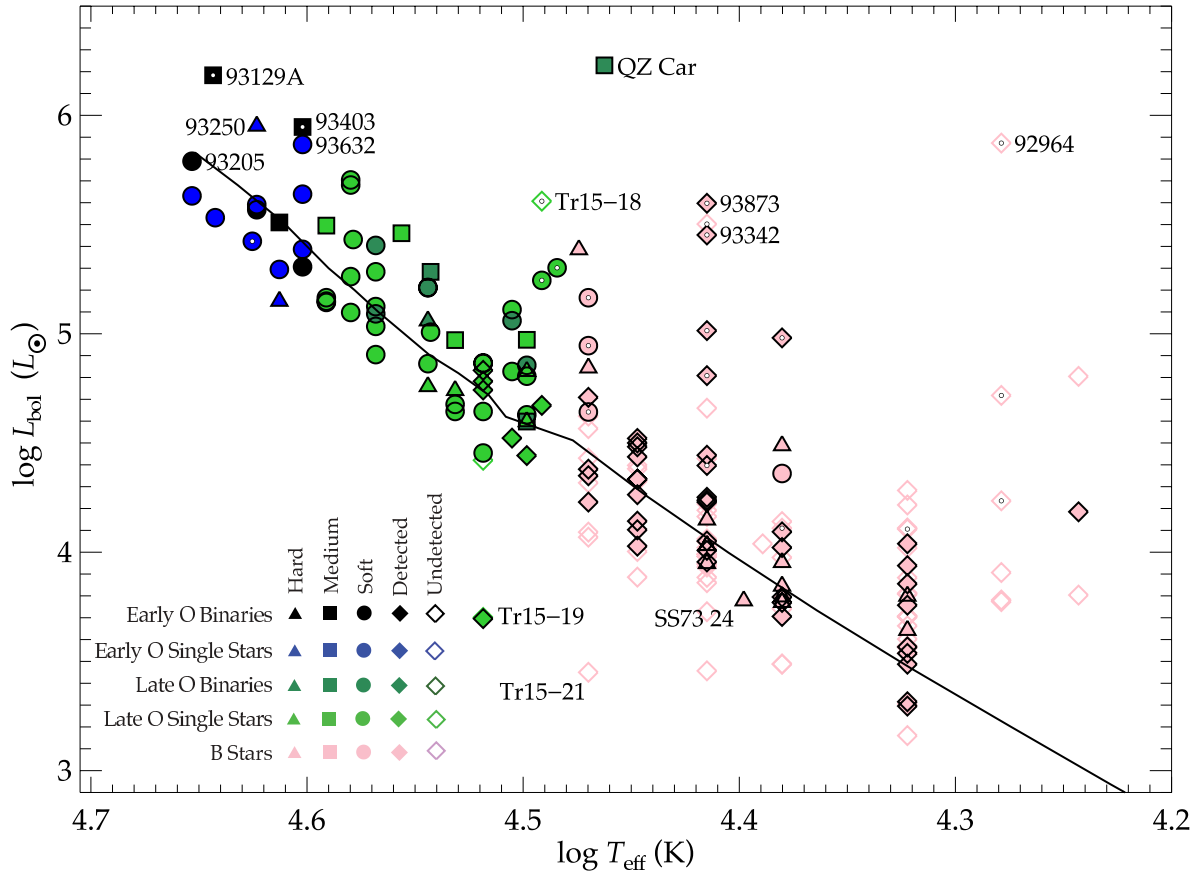
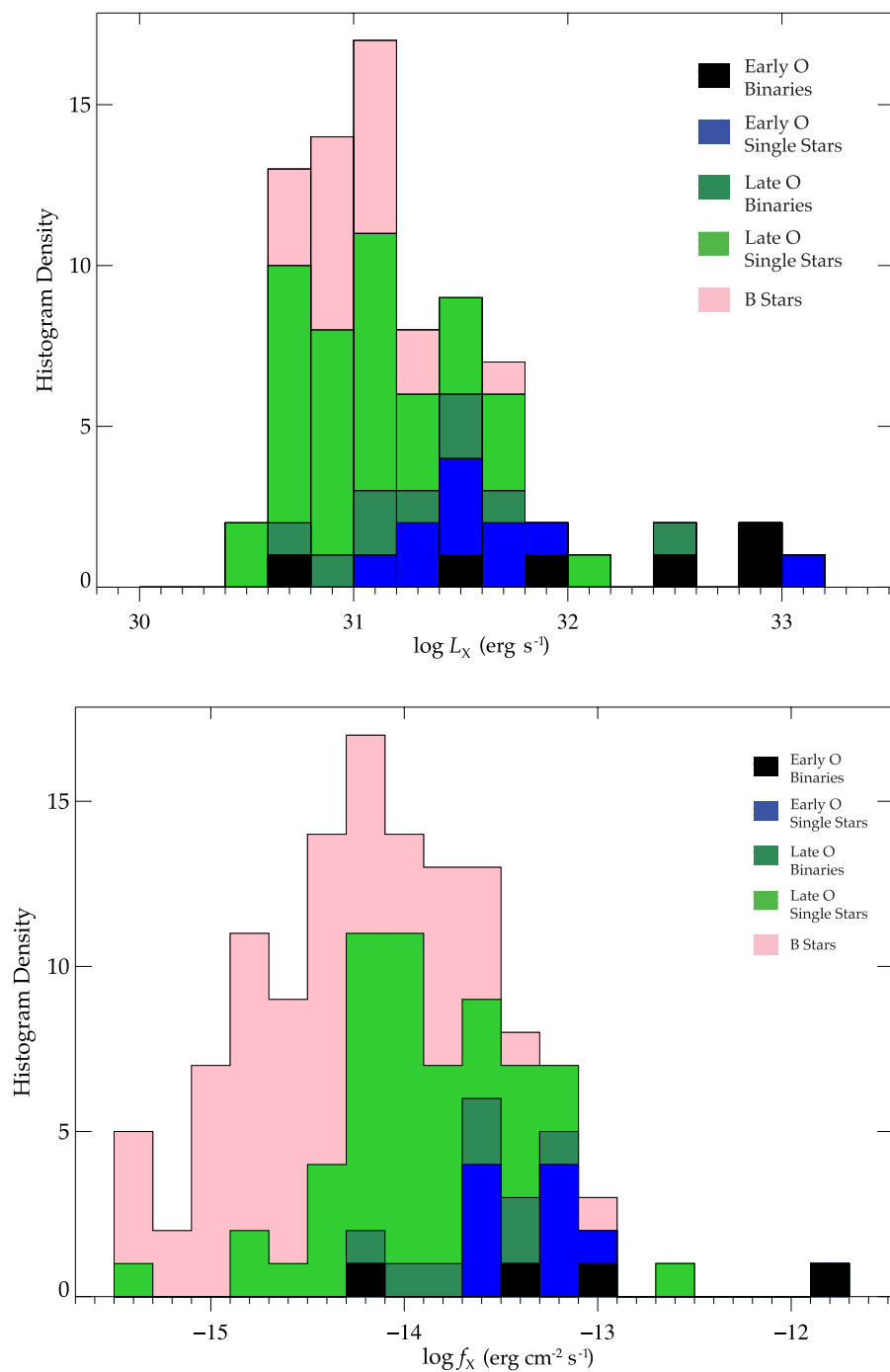


Fig. 2.— HR diagram of the 200 OB stars in the CCCP field of view. See Fig. 1 and §4 for symbol definitions. The most luminous stars are labeled.



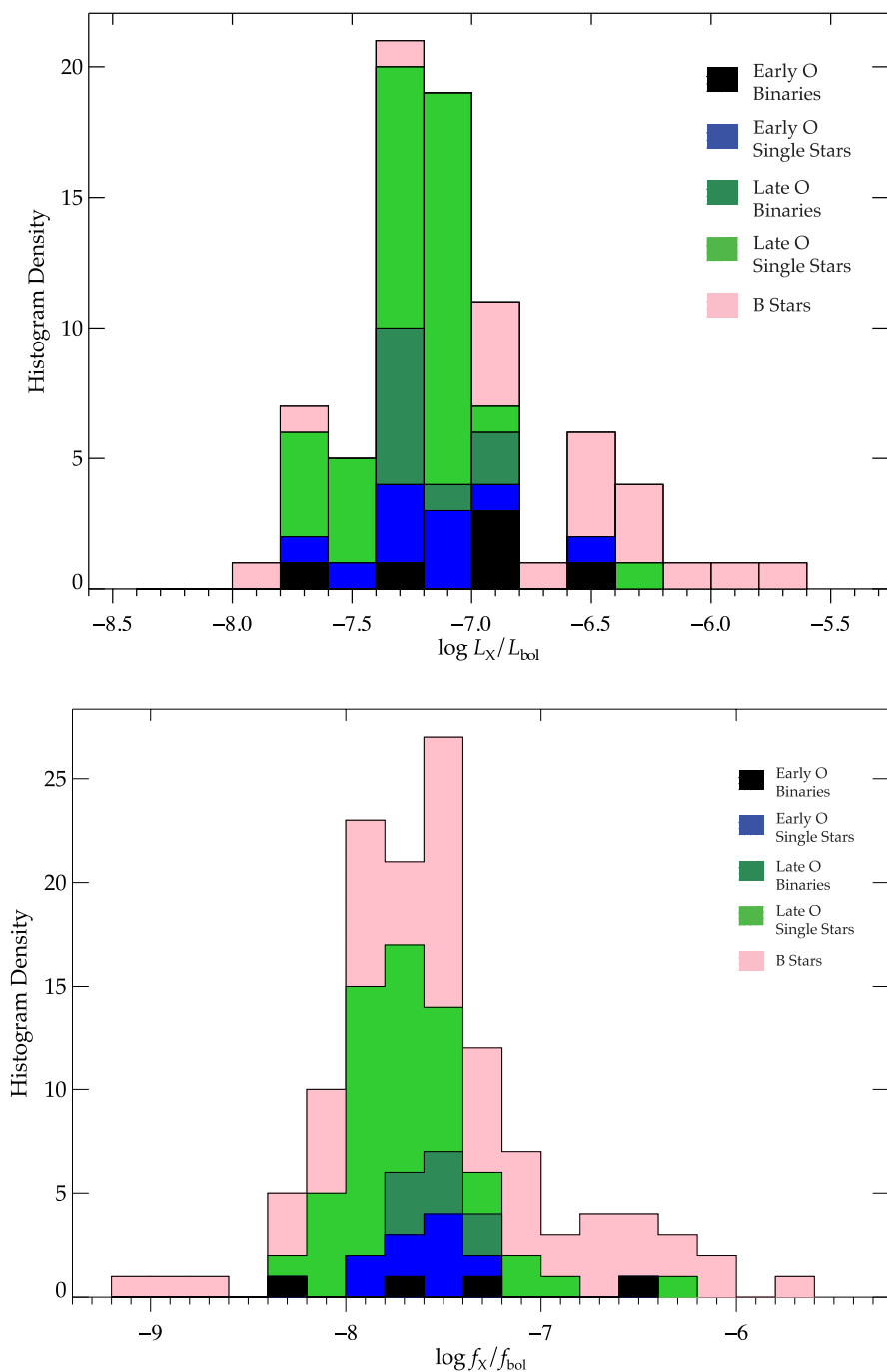


Fig. 6.— *Top panel:* $\log L_X/L_{\text{bol}}$ histogram for the 78 OB stars with XSPEC parameters and more than 50 net ACIS counts. *Bottom panel:* $\log f_X/f_{\text{bol}}$ histogram for the full sample of X-ray detected OB stars.

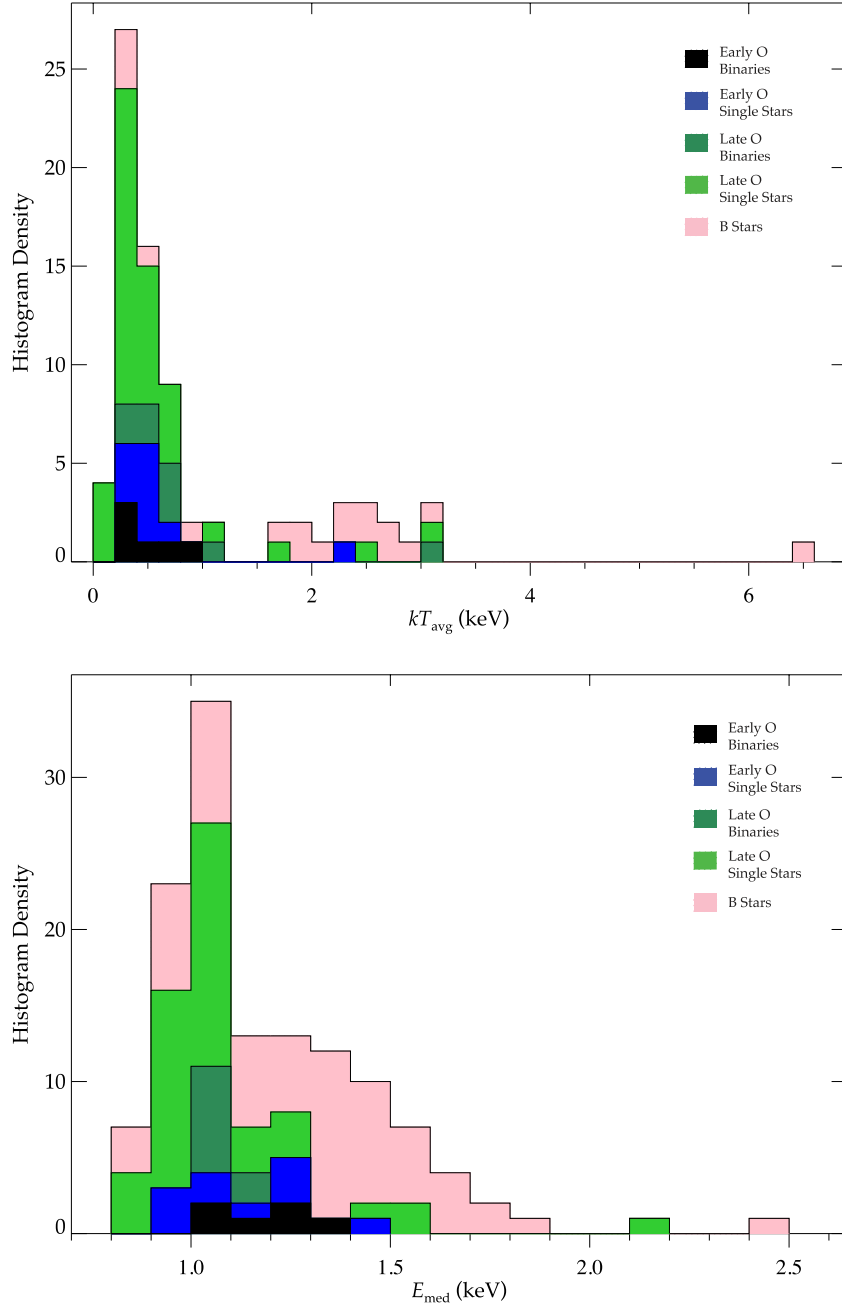


Fig. 7.— *Top panel:* kT_{avg} histogram for the 78 OB stars with XSPEC parameters and more than 50 net ACIS counts. *Bottom panel:* E_{med} histogram for the full sample of X-ray detected OB stars. For the 51 OB stars with fewer than 50 counts and no XSPEC fits, *hard* corresponds approximately to $E_{\text{med}} > 1.5$ keV.

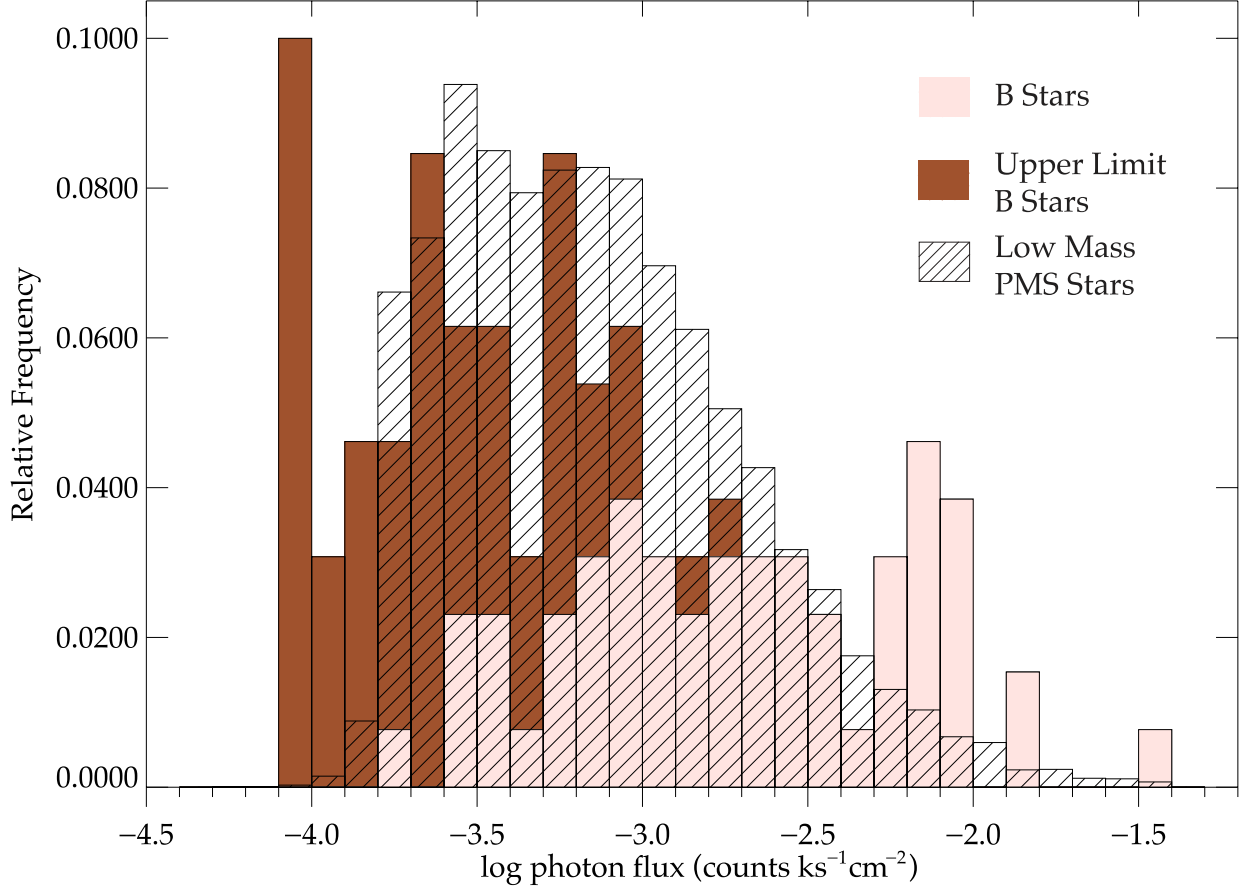


Fig. 8.— Photon flux histogram of the 61 X-ray sources with B-star primaries (in pink), the 69 B-star upper limits (in brown), and the relative frequency of the 14 250 CCCP sources (in gray) with measured photon flux, and not associated with a known massive star (WR or OB star). Most of the 14 250 are associated with lower-mass, coronal, pre-main-sequence stars. This figure and Table 4 suggest two B star populations: a group with log photon flux below -2.3 (corresponding to $\log f_X < -14$) whose X-ray properties are similar to those of the general coronal PMS population, and an active group with log photon flux above -2.3 (corresponding to $\log f_X > -14$), the majority of whose X-rays are probably *not* produced by coronal PMS stars.

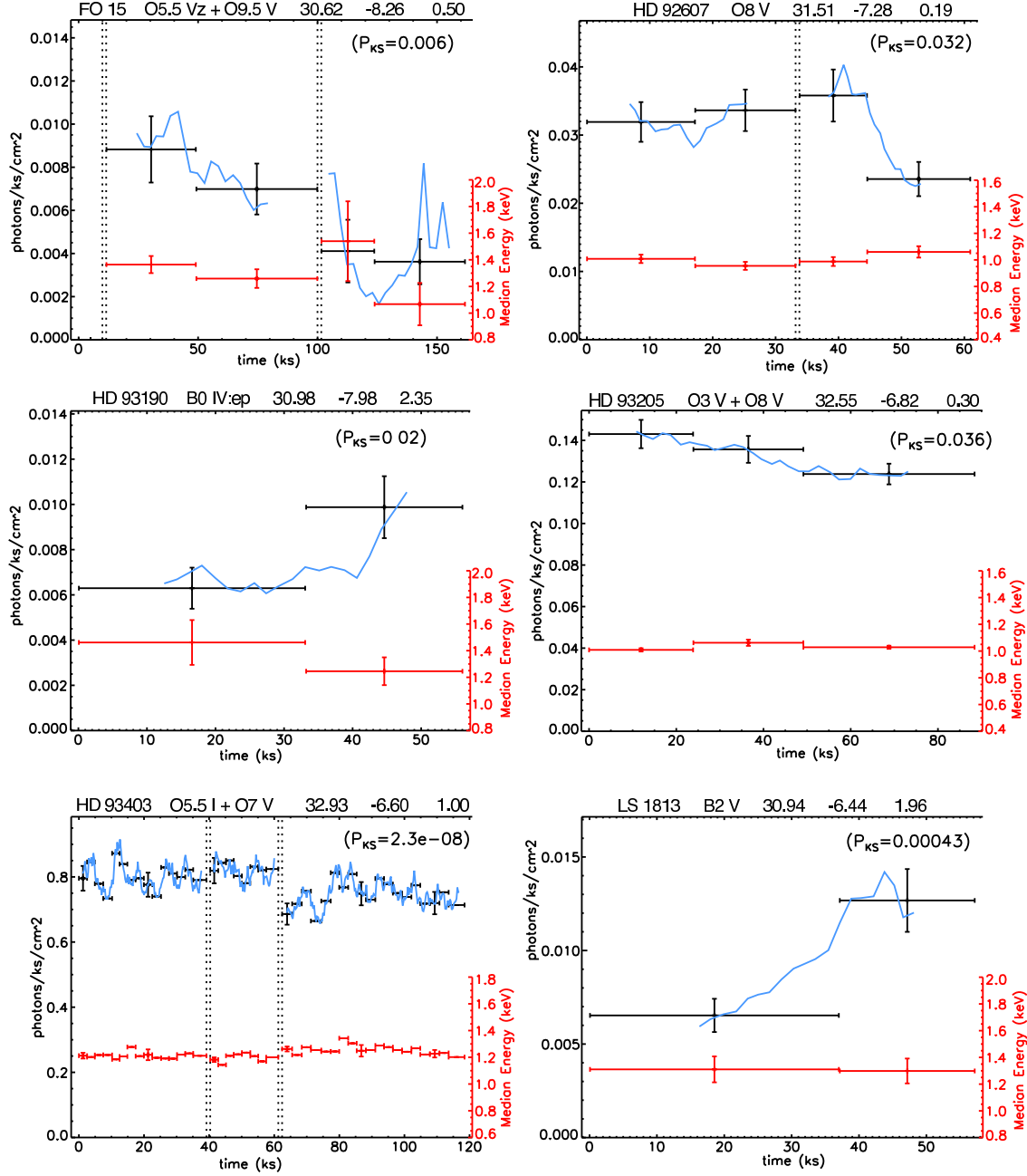


Fig. 9.— Sequenced photon flux light curves of FO 15 (O5.5 Vz + O9.5 V), HD 92607 (O8 V), HD 93190 (B0 IV:ep), HD 93205 (O3 V + O8 V), HD 93403 (O5.5 I + O7 V), and LS 1813 (B2 V). Listed are $\log L_X$, $\log L_X/L_{bol}$, kT_{avg} , and probability of constancy, P_{KS} . The blue curves without error bars are the running count rates, corrected for effective area (in photons $\text{ks}^{-1} \text{cm}^{-2}$). The corrected count rates (in black) and median energy (in red) are binned to show variability. The vertical dotted lines indicated large time gaps between adjacent observations.

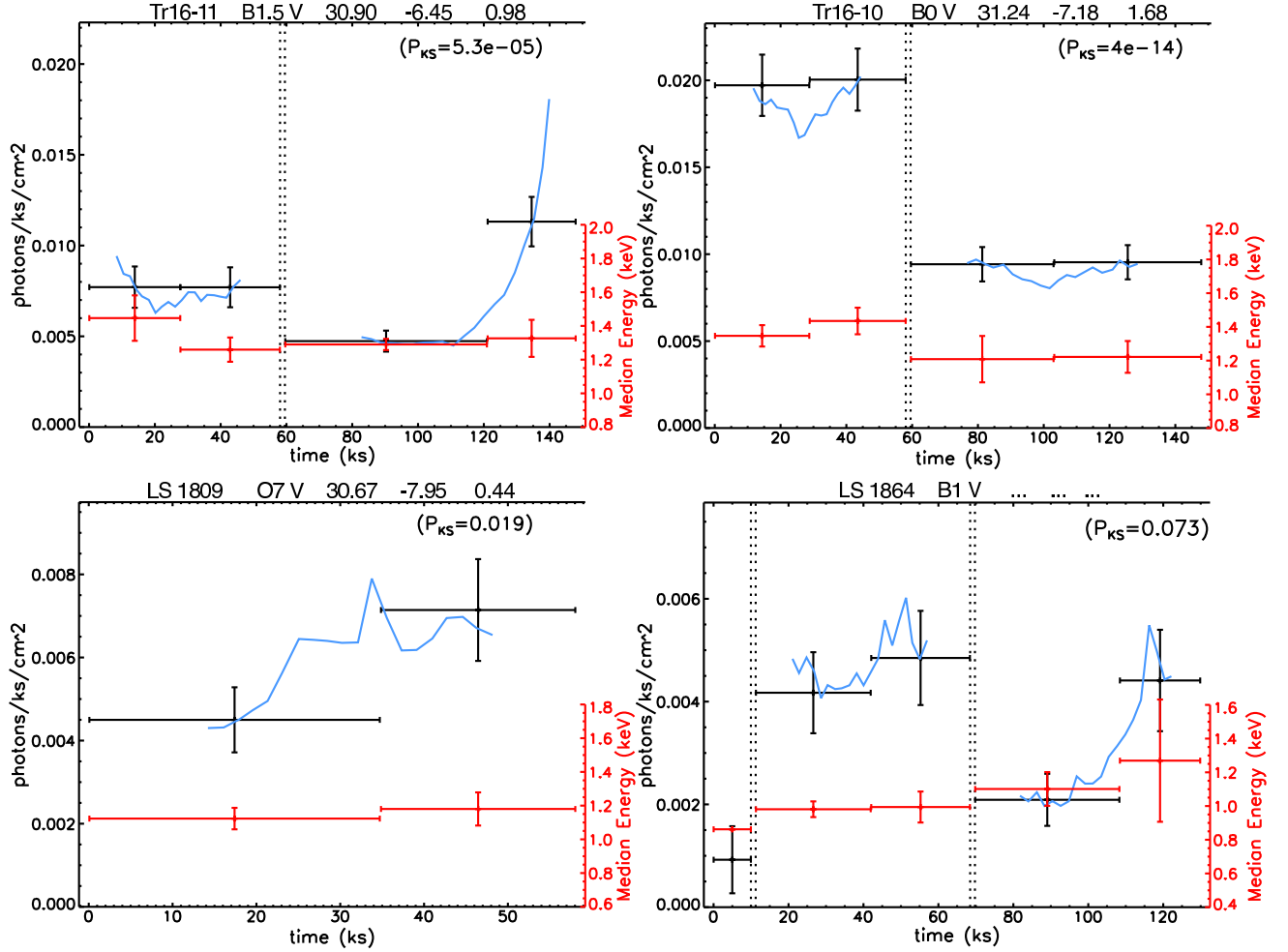


Fig. 10.— Sequenced light curves of Tr16-11 (B1.5 V), Tr16-10 (B0 V), LS 1809 (O7 V), LS 1864 (B1 V). Listed are $\log L_X$, $\log L_X/L_{\text{bol}}$, kT_{avg} , and probability of constancy, P_{KS} . The blue curves without error bars are the running count rates, corrected for effective area (in photons ks⁻¹ cm⁻²). The corrected count rates (in black) and median energy (in red) are binned to show variability. The vertical dotted lines indicated large time gaps between adjacent observations.

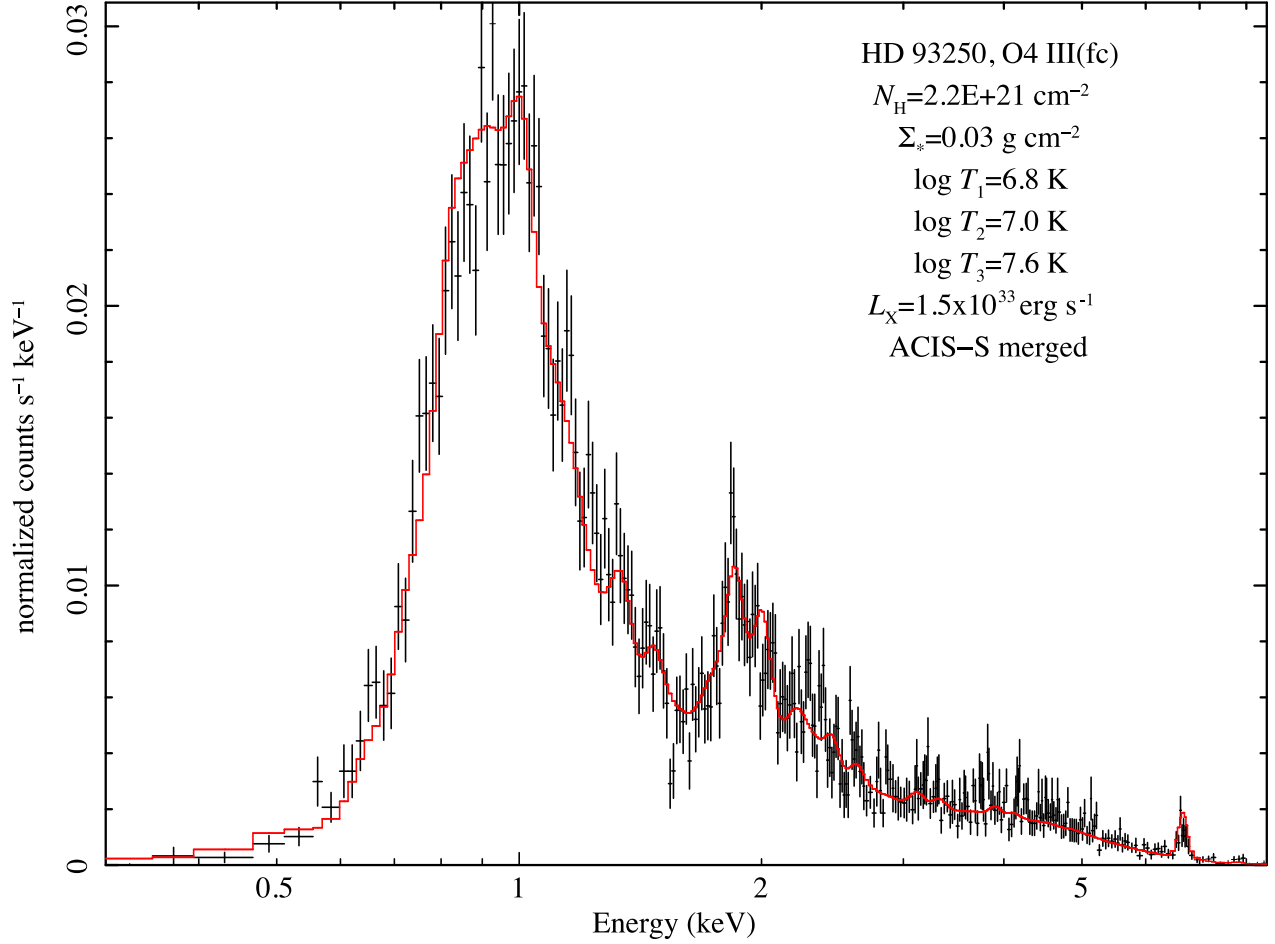


Fig. 11.— Merged off-axis zeroth-order ACIS-S spectrum of HD 93250, O4 III(fc) and best-fit $\text{TBABS}^*(\text{WINDTABS}(\text{APEC})+\text{APEC}+\text{APEC})$ parameters. In this model all three emission components are absorbed by cold, neutral ISM gas, and the 0.5 keV embedded wind shocks are absorbed by warm, partially ionized, solar-abundance plasma distributed throughout the wind. The best-fit mass column is $\Sigma_{*} = 0.03 \pm 0.01 \text{ g cm}^{-2}$.

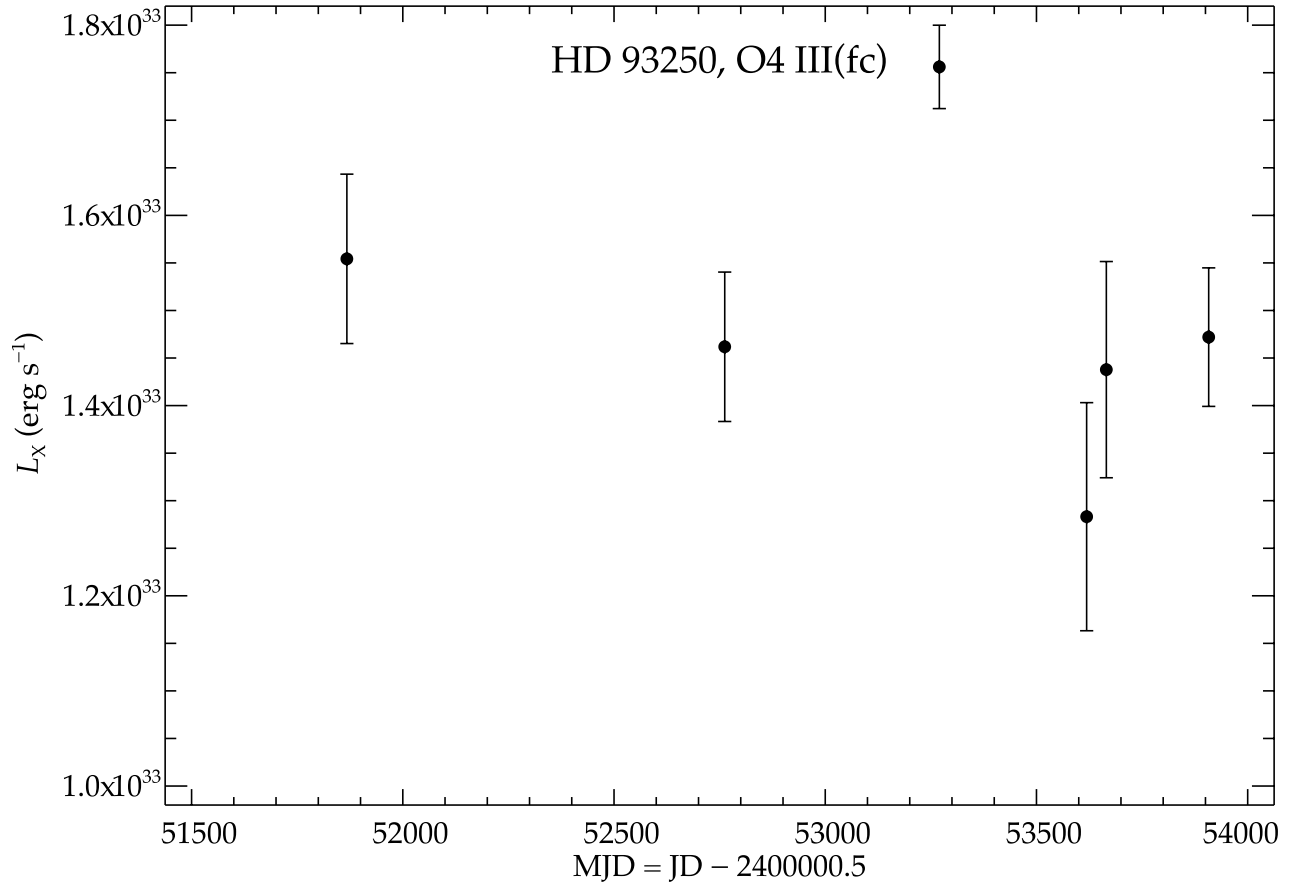


Fig. 12.— L_X light curve of HD 93250, O4 III(fc), assuming the same model as in Fig. 11, indicating significant long-term variability.

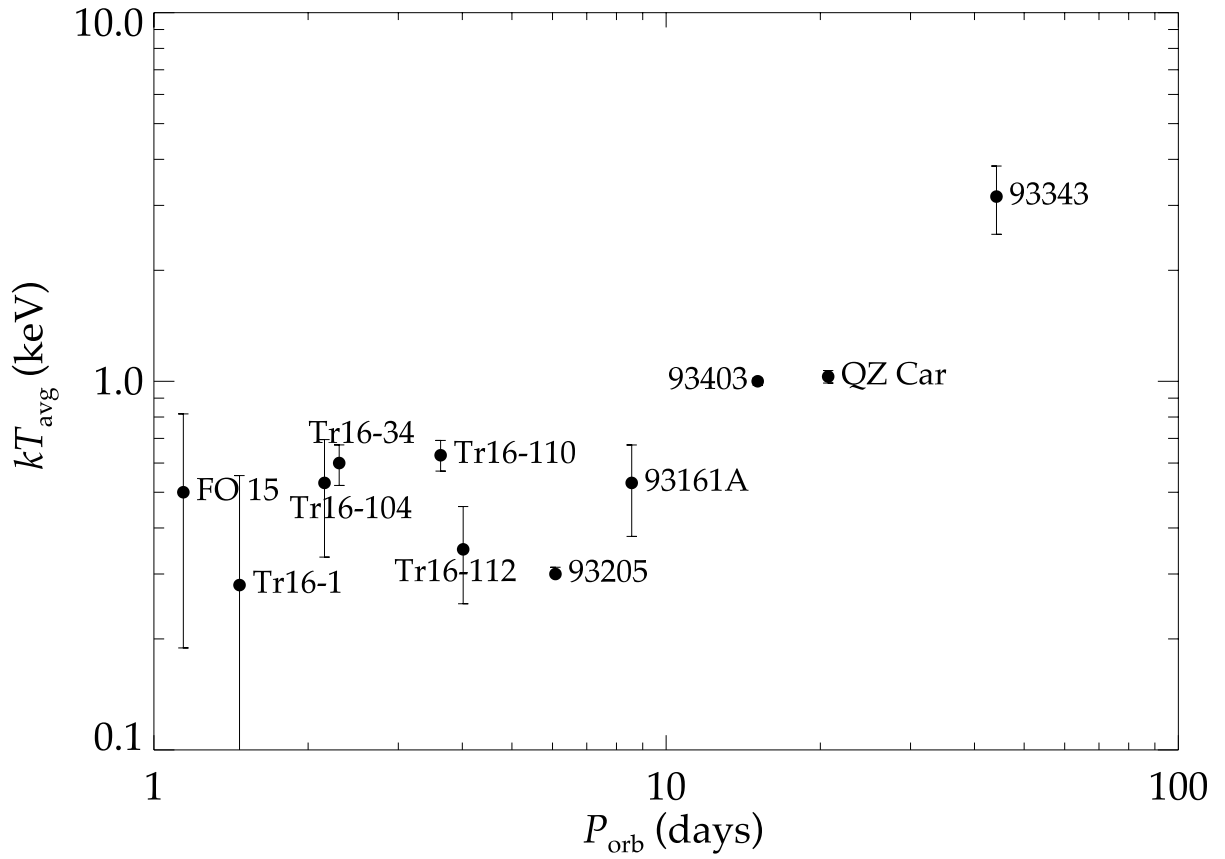


Fig. 13.— kT_{avg} with 90% confidence limits versus primary orbital period for the 11 spectroscopic binaries in Table 3.

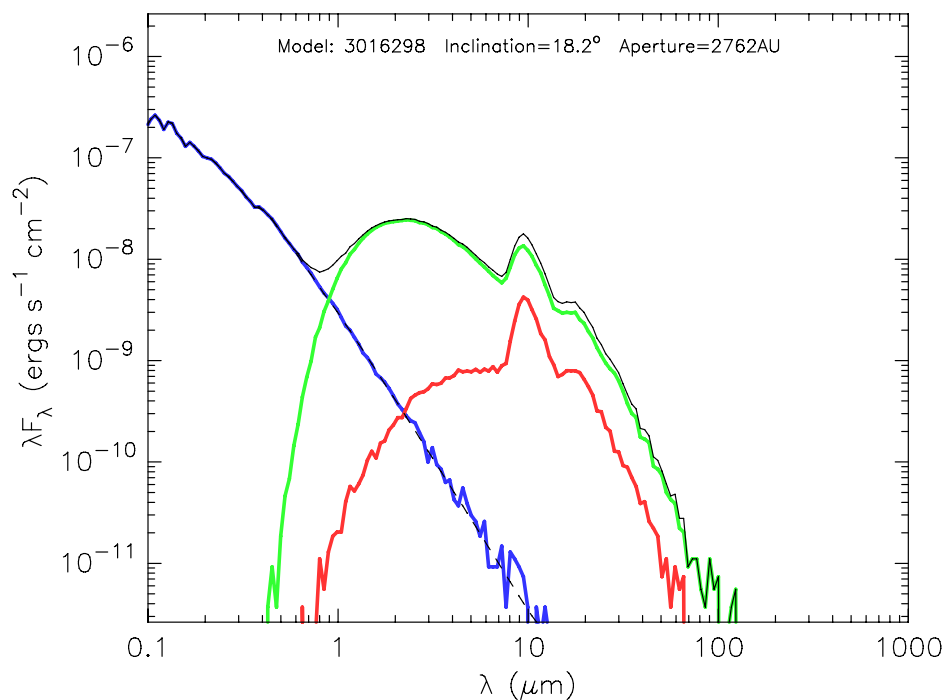
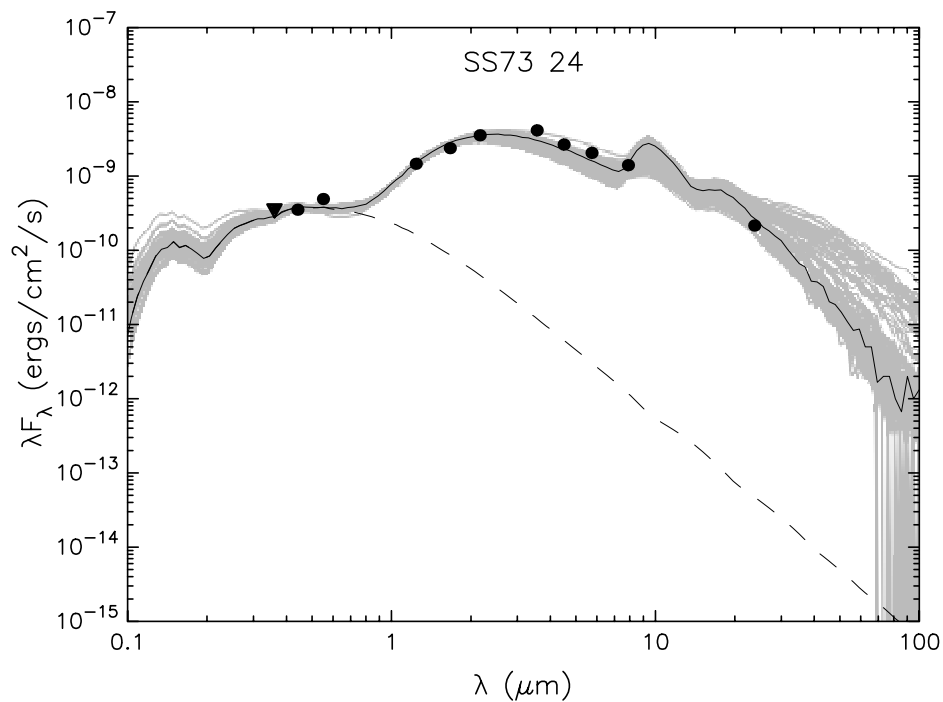


Fig. 14.— *Upper panel:* Optical-infrared SED of SS73 24 and the best-fit (black) Robitaille et al. (2006) YSO model (star + disk + envelope). *Lower panel:* SS73 24’s SED suggests a $6 \pm 2 \times 10^3 L_{\odot}$ photosphere with $T_{\text{eff}} = 25 \pm 1.4$ kK (dashed, blue line), a large disk (solid, green line), and cooler envelope (solid, red line).

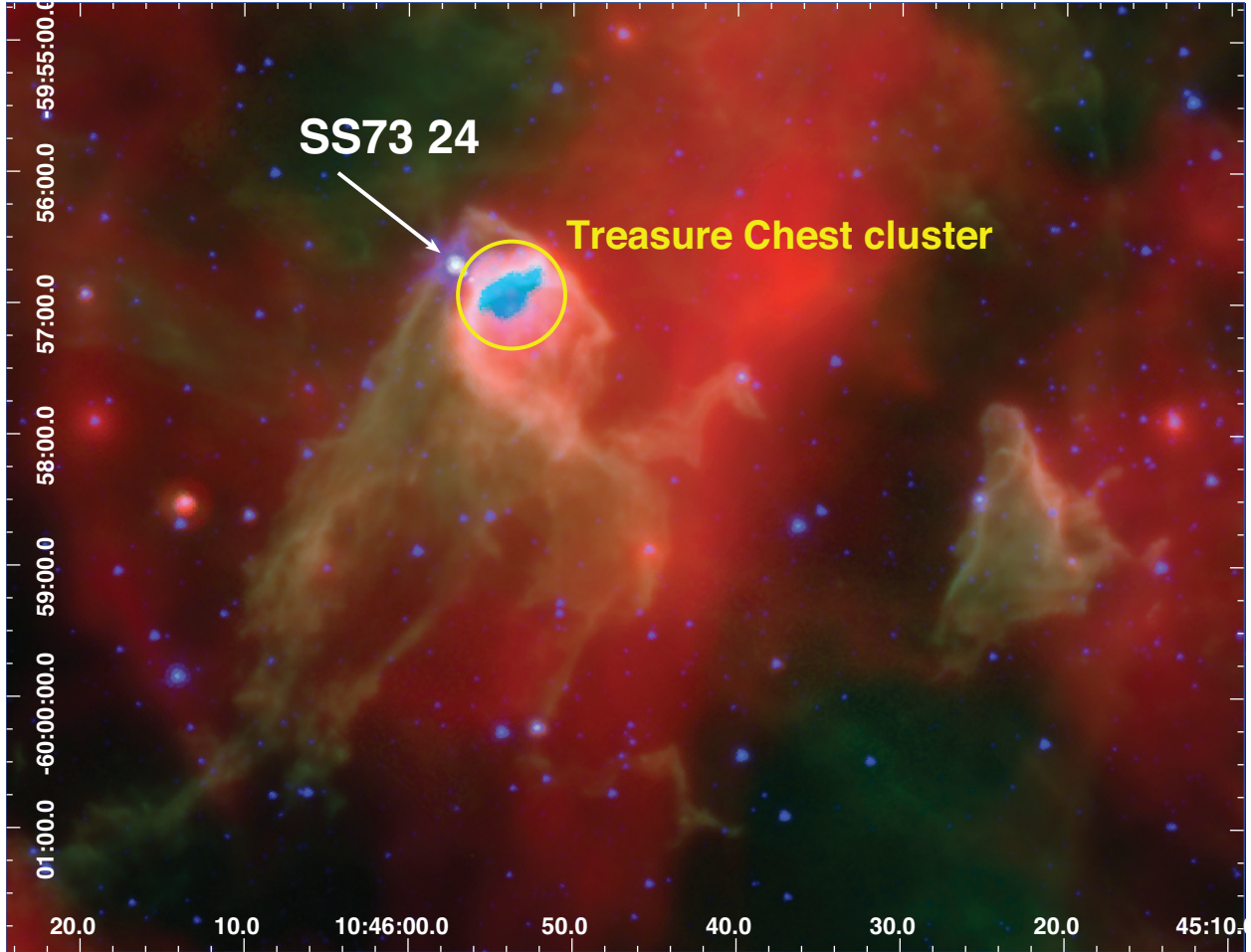


Fig. 15.— *Spitzer* IRAC + MIPS 24 μ m image of SS73 24 and the nearby Treasure Chest cluster. SS73 24’s proximity to the most active star-forming portion of the Treasure Chest suggests it is a very young Herbig Be star.

Table 1. OB Star Catalog: Most Luminous Stars

Star Name	Feinstein	MJ	Other Name	RA. (J2000) Decl.		Spectral Type	V	U - B	B - V	A _V	log $\frac{L_{\text{bol}}}{L_{\odot}}$
QZ Car	Coll 228 33	...	HD 93206	10 44 22.92	-59 59 35.9	O9.7 I + O8 III	6.30	-0.81	0.14	2.21	6.23
HD 93129A	Tr 14 1	MJ 177	CPD-58 2618A	10 43 57.46	-59 32 51.4	O2 If*	7.26	-0.81	0.25	2.32	6.18
HD 93250	Tr 16 180	...	CPD-58 2661	10 44 45.02	-59 33 54.7	O4 III(fc)	7.41	-0.85	0.17	1.87	5.95
HD 93403	CPD-58 2680	10 45 44.11	-59 24 28.2	O5 III(fc) + O7 V	7.27	-0.76	0.22	1.95	5.95
HD 92964	Bo 10 44	...	CPD-58 2581	10 42 40.58	-59 12 56.6	B2.5 Ia	5.38	-0.66	0.26	1.61	5.87
HD 93632	Bo 11 1	...	CPD-59 2696	10 47 12.64	-60 05 50.9	O5 I-III _f	8.36	-0.73	0.30	2.72	5.87
HD 93205	Tr 16 179	MJ 342	CPD-59 2587	10 44 33.75	-59 44 15.4	O3.5 V((f)) + O8 V	7.76	-0.94	0.08	1.60	5.79
HD 93160	Coll 232	MJ 229	CPD-58 2631C	10 44 07.26	-59 34 30.5	O6 III	7.88	-0.68	0.07	2.01	5.70
HD 93130	Coll 228 1	MJ 208	CPD-59 2556	10 44 00.38	-59 52 27.5	O6 III	8.11	-0.75	0.19	2.20	5.68
HD 93843	CPD-59 2732	10 48 37.77	-60 13 25.6	O5 III(fc)	7.32	-0.94	-0.04	1.17	5.64
HD 93128	Tr 14 2	MJ 157	CPD-58 2617	10 43 54.41	-59 32 57.4	O3.5 V((fc))	8.81	-0.79	0.19	2.21	5.63
Tr15-18	Tr 15 18	10 44 36.36	-59 24 20.3	O9 I/II:(e:)	11.28	-0.09	1.11	5.66	5.61
HD 93873	CPD-58 2747	10 48 55.21	-59 26 48.3	B1 Ia	7.74	-0.50	0.45	2.60	5.60
HD 305525	Coll 228 98	MJ 661	CPD-59 2665	10 46 05.70	-59 50 49.4	O4 V	10.03	-0.22	0.57	3.64	5.59
HD 303308	Tr 16 7	MJ 480	CPD-59 2623	10 45 05.92	-59 40 06.1	O4.5 V((fc))	8.19	-0.82	0.14	1.72	5.57
HD 93129B	CPD-58 2618B	10 43 57.65	-59 32 53.8	O3.5 V((fc))	8.84	-0.79	0.23	2.16	5.53
Tr16-112	Tr 16 112	MJ 535	CPD-59 2641	10 45 16.51	-59 43 37.0	O5.5-O6 V(n)((fc)) + B2 V-III	9.28	-0.69	0.29	2.68	5.51
Coll228-12	Coll 228 12	MJ 366	CPD-59 2592	10 44 36.76	-59 54 24.9	B1 Ib	9.52	-0.21	0.68	4.03	5.50
Tr16-100	Tr 16 100	MJ 380	CPD-59 2600	10 44 41.77	-59 46 56.3	O6 V	8.65	-0.77	0.19	2.18	5.50
HD 93222	Coll 228 6	...	CPD-59 2590	10 44 36.25	-60 05 28.9	O7 V((f))	8.10	-0.89	0.05	1.74	5.46
HD 93342	CPD-58 2674	10 45 17.57	-59 23 37.5	B1 Iab-Ib	9.09	-0.40	0.60	3.52	5.45
HD 93161B	10 44 09.09	-59 34 35.4	O6.5 V(f)	8.60	-0.77	0.23	2.10	5.43
Tr16-244	Tr 16 244	MJ 257	...	10 44 13.20	-59 43 10.3	O3/4 If	10.78	-0.32	0.68	4.00	5.42
Tr16-110	Tr 16 110	MJ 517	CPD-59 2636	10 45 12.88	-59 44 19.2	O7 V + O8 V + O9 V	9.31	-0.64	0.29	2.74	5.40
HD 93204	Tr 16 178	MJ 340	CPD-59 2584	10 44 32.34	-59 44 31.0	O5.5 V((fc))	8.48	-0.88	0.09	1.70	5.39
HD 93190	CPD-58 2637	10 44 19.61	-59 16 59.0	B0 IV:ep	8.57	-0.80	0.32	2.38	5.39
FO 15	...	MJ 596	...	10 45 36.32	-59 48 23.4	O5.5 Vz + O9.5 V	12.05	-0.20	0.86	4.96	5.31
HD 305619	CPD-59 2727	10 48 15.54	-60 15 56.9	O9.7 Ib	9.43	-0.55	0.44	3.05	5.30
Coll228-97	Coll 228 97	MJ 691	CPD-59 2673	10 46 22.46	-59 53 20.5	O5 V(n)((f))	10.42	-0.48	0.41	3.28	5.29
HD 93161A	10 44 08.82	-59 34 34.5	O8 V + O9 V	8.56	-0.75	0.20	1.94	5.28
HD 303304	...	MJ 709	CPD-58 2697	10 46 35.69	-59 37 00.6	O7 V	9.71	-0.62	0.33	2.85	5.28
HD 93146	Coll 228 65	...	CPD-59 2555	10 44 00.15	-60 05 09.9	O7 V((f))	8.44	-0.91	0.02	1.46	5.26
HD 305523	Coll 228 32	MJ 336	CPD-59 2580	10 44 29.48	-59 57 18.2	O9 II	8.50	-0.83	0.18	1.97	5.24
HD 92607	CPD-59 2404	10 40 12.42	-59 48 10.0	O8 V	8.23	-0.87	0.00	1.34	5.21
Tr16-34	Tr 16 34	MJ 516	CPD-59 2635	10 45 12.71	-59 44 46.0	O8 V + O9.5 V	9.27	-0.73	0.23	2.37	5.21

Table 1—Continued

Star Name	Feinstein	MJ	Other Name	RA. (J2000) Decl.		Spectral Type	V	U – B	B – V	A_V	$\log \frac{L_{\text{bol}}}{L_{\odot}}$
Tr14-20	Tr 14 20	MJ 115	CPD-58 2611	10 43 46.70	-59 32 54.8	O6 V	9.65	-0.63	0.20	2.35	5.17
HD 305439A	CPD-59 2479A	10 42 10.34	-59 58 00.8	B0 Ia	9.56	-0.52	0.51	2.98	5.17
HD 303311	Tr 16 98	MJ 351	CPD-58 2652	10 44 37.45	-59 32 55.2	O5 V	9.03	-0.86	0.13	1.59	5.15
HD 305532	Coll 228 38	MJ 593	CPD-59 2650	10 45 34.04	-59 57 26.8	O6 V	10.19	-0.70	0.32	2.80	5.15
HD 303316	...	MJ 22	CPD-59 2518	10 43 11.19	-59 44 21.1	O6 V	9.64	-0.76	0.26	2.30	5.14
HD 305524	Coll 228 7	MJ 404	CPD-59 2602	10 44 45.23	-59 54 41.6	O7 V((f))	9.32	-0.75	0.24	2.12	5.12
HD 93249	Tr 15 1	...	CPD-58 2659	10 44 43.88	-59 21 25.0	O9 III	8.36	-0.75	0.14	1.53	5.11
Tr14-8	Tr 14 8	MJ 192	CPD-58 2620	10 43 59.93	-59 32 25.4	O6.5 V	9.45	-0.78	0.05	2.00	5.10
Tr16-104	Tr 16 104	MJ 408	CPD-59 2603	10 44 47.30	-59 43 53.2	O7 V((f)) + O9.5 + B0.2 IV	8.82	-0.79	0.14	1.55	5.09
Tr16-23	Tr 16 23	MJ 484	CPD-59 2626	10 45 05.79	-59 45 19.6	O9 III	10.00	-0.61	0.37	2.91	5.06
HD 93343	Tr 16 182	MJ 512	CPD-59 2633	10 45 12.21	-59 45 00.4	O8 V + O7-8.5 V	9.60	-0.75	0.24	2.33	5.06
LS 1809	CPD-58 2608	10 43 41.24	-59 35 48.2	O7 V	10.44	-0.40	0.50	3.08	5.03
HD 305520	Coll 228 4	...	CPD-59 2560	10 44 05.86	-59 59 41.5	B1 Ib	8.70	-0.71	0.18	2.00	5.01
Tr14-9	Tr 14 9	MJ 165	...	10 43 55.41	-59 32 49.3	O8 V	9.73	-0.68	0.32	2.42	5.01

Table 2. Single O Stars: XSPEC and time variability parameters

Star Name	ACIS Name	Spectral Type	$\log L_X^\#$ (erg s ⁻¹)	$\log \frac{L_X}{L_{\text{bol}}}$	kT_{avg} (keV)	$\log \frac{f_X}{f_{\text{bol}}}^\spadesuit$	P_{KS} (%)*	MLB [†]
Tr16-22	104508.23-594607.0	O8.5 V	32.25	-6.30	1.70	-6.39	14	1
HD 93250 [‡]	104445.04-593354.6	O4 III(fc)	33.12	-6.41	2.30	...	20	1
LS 1865	104454.70-595601.8	O8.5 V((f))	31.42	-6.90	3.09	-7.12	6	3
HD 303311	104437.47-593255.3	O5 V	31.77	-6.96	0.42	-7.47	33	1
LS 1821	104357.46-600528.3	O8.5 V	31.25	-7.01	0.30	-7.55	74	1
Tr16-100	104441.80-594656.4	O6 V	32.06	-7.02	0.35	-7.44	88	1
Tr14-20	104346.69-593254.7	O6 V	31.71	-7.03	0.34	-7.77	98	1
HD 92607	104012.42-594810.1	O8 V	31.75	-7.04	0.19	-7.42	1	2
Tr14-5	104353.63-593328.4	O9 V	30.98	-7.05	0.67	-7.18	33	1
HD 93146	104400.16-600509.8	O7 V((f))	31.77	-7.07	0.24	-7.52	50	1
HD 93129B	104357.65-593253.7	O3.5 V((fc))	32.03	-7.08	0.51	-7.56	84	1
CPD-59 2661	104553.71-595703.9	O9.5 V	31.08	-7.09	2.40	-7.22	19	1
Tr14-21	104348.70-593324.2	O9 V	31.13	-7.10	0.53	-7.52	48	1
HD 93128	104354.40-593257.4	O3.5 V((fc))	32.11	-7.10	0.39	-7.52	26	3
HD 93222	104436.23-600529.0	O7 V((f))	31.94	-7.11	0.27	-7.59	11	3
HD 93843	104837.74-601325.7	O5 III(fc)	32.08	-7.14	0.40	-7.43	26	2
Tr14-9	104355.36-593248.8	O8 V	31.44	-7.14	0.19	-7.81	39	1
HD 305438	104243.71-595416.6	O8 V((f))	31.17	-7.16	0.38	-7.62	60	3
HD 305536	104411.04-600321.8	O9.5 V	31.24	-7.16	1.01	-7.40	57	1
HD 93160	104407.26-593430.5	O6 III	32.10	-7.18	0.25	-7.68	2	2
Tr16-3	104506.70-594156.6	O8.5 V	31.04	-7.18	0.36	-7.74	49	1
HD 303316	104311.17-594420.8	O6 V	31.53	-7.19	0.30	-7.77	89	1
Tr16-115	104520.57-594251.1	O9.5 V	31.01	-7.20	0.32	-7.65	18	1
Tr14-8	104359.92-593225.4	O6.5 V	31.48	-7.20	0.23	-7.83	89	1
Tr16-244	104413.19-594310.1	O3/4 If	31.80	-7.21	0.62	-7.33	34	1
HD 93028	104315.33-601204.3	O9 IV	31.23	-7.21	0.14	-7.74	10	1
HD 93161B	104409.08-593435.3	O6.5 V(f)	31.75	-7.26	0.54	-7.62	11	1
HD 305524	104445.27-595441.5	O7 V((f))	31.43	-7.28	0.61	-7.60	10	1
HD 305518	104343.99-594817.9	O9.5 V	31.27	-7.29	0.38	-7.96	61	1
HD 93204	104432.34-594431.0	O5.5 V((fc))	31.67	-7.29	0.30	-7.70	9	1
HD 93027	104317.92-600803.1	O9.5 IV	31.08	-7.30	0.27	-7.81	34	1
HD 305539	104633.07-600412.9	O7	31.16	-7.32	0.48	-7.81	25	4
HD 305532	104534.04-595726.7	O6 V	31.39	-7.34	0.23	-7.88	83	1
LS 1892	104622.48-595320.4	O5 V(n)((fc))	31.53	-7.35	0.55	-7.64	47	2
HD 93249	104443.88-592125.1	O9 III	31.33	-7.36	0.46	-7.69	45	1
HD 305525	104605.70-595049.5	O4 V	31.76	-7.41	0.33	-7.92	41	1
HD 305523	104429.47-595718.1	O9 II	31.41	-7.41	0.30	-8.06	9	1
Tr16-21	104436.73-594729.5	O8 V	30.97	-7.47	0.15	-7.91	14	1
HD 93576	104653.84-600441.9	O9 IV	30.91	-7.50	0.34	-7.86	86	1
LS 1809	104341.24-593548.1	O7 V	31.03	-7.58	0.44	-7.93	1	2
HD 93130	104400.38-595227.5	O6 III	31.65	-7.61	0.63	-8.00	33	1
HD 303304	104635.70-593700.7	O7 V	31.23	-7.64	0.74	-7.87	7	1
HD 305612	104716.41-600539.9	O9 V	30.80	-7.64	0.54	-7.93	94	1
HD 93632	104712.63-600550.8	O5 I-IIIf	31.77	-7.67	0.56	-7.92	94	1
HD 305619	104815.50-601556.9	O9.7 Ib	31.20	-7.68	0.54	-8.18	68	1

Table 2—Continued

Star Name	ACIS Name	Spectral Type	$\log L_X^\ddagger$ (erg s^{-1})	$\log \frac{L_X}{L_{\text{bol}}}$	kT_{avg} (keV)	$\log \frac{f_X}{f_{\text{bol}}}$ \spadesuit	P_{KS} (%)*	MLB †
Tr15-19	104435.91-592335.7	O9 V	-6.85	10	...
CPD-58 2627	104402.44-592936.3	O9 III	-7.67	1	...
Coll228-67	104400.43-600559.8	O9 V	-7.80	29	...
Bo11-5	104715.29-600538.8	O9 V:	-8.04	11	...
Tr14-127	104400.94-593545.7	O9 V	-8.07	33	...
Coll228-66	104359.45-600513.3	O9.5 V	-8.10
Tr15-2	104443.77-592117.2	O9.5 III:	-8.32	19	...
Tr14-27	104343.89-593346.1	O9 V	-8.98
Tr15-18	104436.35-592420.3	O9 I/II:(e:)
Tr15-20	104435.12-592328.1	O9 V:

*Kolmogorov-Smirnov percent probability of constancy. Minimum of single-epoch and merged P_{KS} values.

† Number of distinct maximum likelihood blocks in merged event data (minimum 5 counts per block, 95% confidence).

‡ HD 93250 was piled up in the ACIS-I CCCP survey data: f_X not computed in ACIS EXTRACT. L_X is the mean value observed in a series of off-axis zeroth-order grating observations. See Figs. 11 and 12 and Appendix A.

§ The ISM-corrected 0.5-8 keV L_X , FITLUMINOSITY_TC. For the ISM-corrected 0.5-10 keV L_X , see Nazé et al. (2011).

$\spadesuit f_X$ is the absorbed (uncorrected) 0.5-8.0 keV flux, ENERGYFLUX_T. For the absorbed 0.5-10 keV flux, FTO see Nazé et al. (2011).

Table 3. O+O Binaries: XSPEC and time variability parameters

Star Name	ACIS Name	Spectral Type	P_{orb}^{\dagger} (days)	$\log L_X^{\ddagger}$ (erg s $^{-1}$)	$\log \frac{L_X}{L_{\text{bol}}}$	kT_{avg} (keV)	P_{KS} (%)*	MLB ‡
HD 93403	104544.13-592428.1	O5 III(fc) + O7 V	15.093	33.11	-6.41	1.00	9	3
HD 93205	104433.74-594415.4	O3 V + O8 V	6.0803	32.55	-6.82	0.30	3	1
HD 93129A	104357.47-593251.3	O2 If*•	...	32.91	-6.85	0.74	46	1
HD 303308	104505.90-594006.0	O4.5 V((fc))•	...	32.25	-6.89	0.25	20	4
HD 93161A	104408.84-593434.4	O8 V + O9 V	8.566	31.94	-6.92	0.53	81	1
HD 93343	104512.23-594500.5	O8 V + O7-8.5 V	44.15	31.66	-6.98	3.17	30	1
Tr16-9	104505.84-594307.7	O9.5 V•	...	31.27	-7.17	0.70	9	2
Tr16-34	104512.72-594446.2	O8 V + O9.5 V	2.30000	31.56	-7.23	0.60	26	5
Tr16-110	104512.88-594419.3	O7 V + O8 V + O9 V	3.62864, 5.034	31.74	-7.24	0.63	19	4
QZ Car	104422.91-595935.9	O9.7 I + O8 III	20.72, 5.999	32.55	-7.26	1.03	5	1
Tr16-23	104505.79-594519.7	O9 III•	...	31.38	-7.26	0.32	83	1
Tr16-104	104447.31-594353.3	O7 V((f)) + O9.5 + B0.2 IV	2.1529	31.38	-7.29	0.53	49	1
Tr16-1	104508.21-594049.6	O9.5 V + B0.3 V	1.4693	30.87	-7.30	0.28	38	1
Tr16-112	104516.52-594337.1	O5.5-O6 V(n)((fc)) + B2 V-III	4.0157	31.78	-7.31	0.35	53	1
FO 15	104536.33-594823.5	O5.5 Vz + O9.5 V	1.1414	31.24	-7.65	0.50	41	5

*Kolmogorov-Smirnov percent probability of constancy. Minimum of single-epoch and merged P_{KS} values.

† Orbital period(s) in days (Rauw et al. 2009, Nelan et. 2010). For triple and quadruple systems the primary period is shown in Fig. 13.

‡ Number of distinct maximum likelihood blocks in merged data (minimum 5 counts, 95% confidence).

•Close visual binary detected with *HST* FGS by Nelan et al. (2004, 2010).

‡ The ISM-corrected 0.5-8 keV L_X , FITLUMINOSITY_TC. For the ISM-corrected 0.5-10 keV X-ray luminosity, see Nazé et al. (2011).

Table 4. Notable Early B stars: XSPEC and time variability parameters

Star Name	ACIS Name	Spectral Type	$\log L_X^\ddagger$ (erg s ⁻¹)	$\log \frac{L_X}{L_{\text{bol}}}$	kT_{avg} (keV)	$\log f_X^\clubsuit$ (erg cm ⁻² s ⁻¹)	P_{KS} (%)*	MLB [†]
SS73 24	104557.13-595643.1	Be pec	31.70	-5.65	3.13	-13.07	19	2
Tr16-64	104504.75-594053.7	B1.5 Vb	31.37	-6.05	2.73	-13.48	30	2
Tr16-10	104430.34-593726.8	B0 V	31.44	-6.99	1.68	-13.56	32	2
Tr16-5	104454.06-594129.4	B1 V	31.18	-6.43	2.94	-13.64	0	4
Tr14-28	104343.55-593403.4	B2 V	31.24	-5.98	2.74	-13.66	0	3
HD 93501	104622.02-600118.8	B1.5 III:	31.13	-6.94	> 6.	-13.69	30	1
Coll228-68	104400.17-600607.7	B1 Vn	31.06	-6.46	2.54	-13.76	2	3
Tr14-124	104405.84-593511.6	B1 V	31.13	-6.59	1.96	-13.77	12	2
HD 93190	104419.63-591658.6	B0 IV:ep	31.12	-7.84	2.35	-13.77	1	2
Tr14-18	104357.96-593353.4	B1.5 V	31.13	-6.25	2.13	-13.77	40	1
LS 1813	104345.04-595325.0	B2 V	31.04	-6.34	1.96	-13.81	0	2
Tr16-11	104422.51-593925.4	B1.5 V	31.00	-6.35	0.98	-13.88	0	4
Tr14-19	104358.45-593301.5	B1 V	31.07	-6.54	2.38	-13.92	92	1
HD 92644	104031.71-594643.9	B1.5 III	31.12	-6.82	0.24	-13.98	52	1
Tr14-29	104405.09-593341.4	B1.5 V	30.91	-6.62	2.49	-14.02	16	2
HD 305533	104513.44-595753.1	B0.5 Vnn: (shell)	-14.16	20	1
HD 305599	104924.95-594944.0	B0 Ib	31.28	-6.94	0.23	-14.19	17	2
HD 305439A	104210.35-595800.9	B0 Ia	31.11	-7.63	0.56	-14.20	7	2
Tr16-126	104359.86-593524.1	B1 V	-14.24	66	2
HD 305538	104546.52-600513.5	B0 V	-14.27	30	3
HD 305556	104343.42-602027.7	B0 Ib	31.17	-7.36	0.28	-14.27	9	1
Tr14-22	104348.82-593335.2	B2 V	-14.33	64	1
HD 92741	104112.33-595825.0	B1.5 II:	-14.64	2	2
LS 1864	104450.39-595545.0	B1 V	-14.70	7	1
HD 93026	104316.35-591027.2	B1.5 V	-14.82	6	1
HD 303225	104135.44-593945.6	B1.5 V	-14.90	9	1
HD 305606	104925.87-600137.3	B2 V	-14.92	1	1

*Kolmogorov-Smirnov percent probability of constancy. Minimum of single-epoch and merged P_{KS} values.

[†]Number of distinct maximum likelihood blocks in merged event data (minimum 5 counts, 95% confidence).

[‡]HD 93501's 160-count spectrum can be fit with a power law or $kT > 6.5$ keV (90% confidence) (Nazé et al. 2011).

[§]The ISM-corrected 0.5-8 keV L_X , FITLUMINOSITY_TC. For the ISM-corrected 0.5-10 keV X-ray luminosity, see Nazé et al. (2011).

[♣] f_X is the absorbed (uncorrected) 0.5-8.0 keV flux, ENERGYFLUX_T. For the absorbed 0.5-10 keV flux, FTO see Nazé et al. (2011).

Table 5. *Chandra* Observations of HD 93250

Date	MJD	Grating	OBSID	Exposure
2000-11-19	51867.12	HETG	632	89545.8
2003-05-02	52761.50	HETG	3745	94533.0
2004-09-21	53269.73	NONE	4495	56634.4
2005-09-05	53618.62	HETG	5400	33727.4
2005-10-22	53665.13	HETG	5399	39670.4
2006-06-19	53905.75	HETG	7341	53265.7
2006-06-22	53908.43	HETG	7342	49313.2
2006-06-23	53909.74	HETG	7189	17721.5